



Liu, E., Cashman, K., Rust, A., & Edmonds, M. (2018). Insights into the dynamics of mafic magmatic-hydromagmatic eruptions from volatile degassing behaviour: The Hverfjall Fires, Iceland. *Journal of Volcanology and Geothermal Research*, 358, 228-240.  
<https://doi.org/10.1016/j.jvolgeores.2018.05.016>

Peer reviewed version

License (if available):  
CC BY-NC-ND

Link to published version (if available):  
[10.1016/j.jvolgeores.2018.05.016](https://doi.org/10.1016/j.jvolgeores.2018.05.016)

[Link to publication record in Explore Bristol Research](#)  
PDF-document

This is the author accepted manuscript (AAM). The final published version (version of record) is available online via Elsevier at <https://www.sciencedirect.com/science/article/pii/S0377027318300398> . Please refer to any applicable terms of use of the publisher.

## University of Bristol - Explore Bristol Research

### General rights

This document is made available in accordance with publisher policies. Please cite only the published version using the reference above. Full terms of use are available:  
<http://www.bristol.ac.uk/red/research-policy/pure/user-guides/ebr-terms/>

# Insights into the dynamics of mafic magmatic-hydromagmatic eruptions from volatile degassing behaviour: The Hverfjall Fires, Iceland

E.J. Liu<sup>\*1</sup>, K.V. Cashman<sup>2</sup>, A.C. Rust<sup>2</sup> & M. Edmonds<sup>1</sup>

<sup>1</sup>Department of Earth Sciences, University of Cambridge, Downing Street, Cambridge, CB2 3EQ, UK.

<sup>2</sup>School of Earth Sciences, University of Bristol, Wills Memorial Building, Bristol, BS81RJ, UK.

\*Corresponding author: E.J.L (ejl54@cam.ac.uk)

## Abstract

The style and intensity of hydromagmatic activity is governed by a complex interplay between the relative volumes of magma and water that interact, their relative viscosities, the depth of subsurface explosions, the substrate properties, and the vent geometry. Fundamental questions remain, however, regarding the role of magmatic vesiculation in determining the dynamics of magma-water interaction (MWI). Petrological reconstructions of magmatic degassing histories are commonly employed to interpret the pre- and syn-eruptive conditions during ‘dry’ magmatic eruptions, but the application of similar techniques to hydromagmatic activity has not yet been fully explored. In this study, we integrate glass volatile measurements (S, Cl, H<sub>2</sub>O and CO<sub>2</sub>) with field observations and microtextural measurements to examine the relationship between degassing and eruptive style during the Hverfjall Fires fissure eruption, Iceland. Here, coeval fissure vents produced both ‘dry’ magmatic (Jarðbaðshólar scoria cone complex) and variably wet hydromagmatic (Hverfjall tuff ring) activity, generating physically distinct pyroclastic deposits with contrasting volatile signatures. Matrix glass volatile concentrations in hydromagmatic ash ( $883 \pm 172$  [1 $\sigma$ ] ppm S;  $0.45 \pm 0.03$  [1 $\sigma$ ] wt% H<sub>2</sub>O;  $\leq 20$  ppm CO<sub>2</sub>) are consistently elevated relative to magmatic ash and scoria lapilli ( $418 \pm 93$  [1 $\sigma$ ] ppm S;  $0.12 \pm 0.48$  [1 $\sigma$ ] wt% H<sub>2</sub>O; CO<sub>2</sub> below detection) and overlap with the range for co-erupted

phenocryst-hosted melt inclusions ( $1522 \pm 127$  [1 $\sigma$ ] ppm S;  $165 \pm 27$  [1 $\sigma$ ] ppm Cl). Measurements of hydromagmatic glasses indicate that the magma has degassed between 17 and 70% of its initial sulfur prior to premature quenching at variably elevated confining pressures.

By comparing volatile saturation pressures for both magmatic and hydromagmatic glasses, and how these vary through the eruptive stratigraphy, we place constraints on the conditions of MWI. Crucially, our data demonstrate that the magma was already vesiculating when it encountered groundwater at depths of 100–200 m, and that the external water supply was sufficient to maintain MWI throughout the eruption with no significant vertical or lateral migration of the fragmentation surface. We propose that development of an in-vent water-sediment slurry provides a mechanism through which the elevated confining pressures of ~1.6–2.6 MPa (or up to 6 MPa accounting for uncertainty in CO<sub>2</sub> below analytical detection) could be maintained and buffered throughout the eruption, whilst enabling vertical mixing and ejection of fragmented juvenile and lithic material from a range of depths. Importantly, these results demonstrate that the volatile contents of hydromagmatic deposits provide valuable records of (1) the environment of MWI (e.g., groundwater versus surface water, vertical migration of the fragmentation level) and (2) the state of the magma at the time of fragmentation and quenching. We further suggest that the volatile content of tephra glasses provides a reliable alternative (or additional) indicator of a hydromagmatic origin, particularly for reduced Ocean Island Basalts where late-stage volatile saturation and degassing (S, H<sub>2</sub>O) occurs over a pressure range relevant to typical MWI environments.

## **Keywords**

hydromagmatism, Hverfjall Fires, Iceland, volatiles

## 1. Introduction

Hydromagmatic eruptions are generated by the explosive interaction of magma with external water. In contrast to ‘dry’ basaltic eruptions that are driven purely by the rapid exsolution and expansion of magmatic volatiles (Mangan and Cashman, 1996; Parfitt, 1998; Mangan et al., 2014), the energy released during magma-water interaction (MWI) is further influenced by the efficiency of heat exchange with water and/or steam. Energetic water vaporisation/expansion during MWI causes extensive melt fragmentation, which is enhanced by the brittle response of silicate melt to rapid quenching (e.g., Lorenz, 1975; Peckover et al., 1973; Colgate and Sigurgeirsson, 1973; Sheridan and Wohletz, 1983; Kokelaar, 1986; Wohletz, 1986; Zimanowski et al., 1991, 1997; Büttner et al., 2002; Van Otterloo et al., 2015; Cashman and Scheu, 2015; Liu et al., 2015, 2017). High vesicularities and bubble number densities within some hydromagmatic pyroclasts demonstrate that significant vesiculation can take place prior to MWI (Mastin et al., 2004; Murtagh et al., 2011; Rausch et al., 2015; Liu et al., 2015, 2017), with the shape and size distributions of fragmented particles determined by the bubble population at the time of quenching and brittle fragmentation. Magma ascent histories and degassing budgets can be reconstructed from the volatile concentrations preserved within pristine melt inclusions and the matrix glass of erupted pyroclasts (e.g., Þórðarson et al., 1996; Metrich et al., 1991, 2010; Þórðarson and Self, 2003; Wallace 2003; Edmonds, 2008; Metrich and Wallace, 2008; Self et al., 2008; Johnson et al., 2010; Wallace and Edmonds, 2011; Hartley et al., 2014; Wallace et al., 2015). Yet, similar geochemical approaches to explore the dynamics of MWI remain comparatively under-utilised.

Mixed eruptions including both magmatic and hydromagmatic phases (either at a single vent or at different vents along an active fissure) are common in Iceland due to the abundance of external water sources within volcanic environments. Icelandic tephra erupted during hydromagmatic and magmatic activity have distinct residual volatile compositions, with matrix



glass sulfur concentrations ( $S_{MG}$ ) consistently elevated within hydromagmatic pyroclasts (Þórðarson et al., 1996, 2001, 2003; Óladóttir et al., 2008; Sigmarsson et al., 2013; Schipper et al., 2015). The Laki fissure eruption of 1783–84 provides an illustrative example of a mixed eruption: hydromagmatic tephra comprises ~20% of the total tephra volume, with the remainder produced by ‘dry’ Strombolian activity. Laki hydromagmatic glasses contain variable but elevated  $S_{MG}$  (490–1260 ppm; average  $933 \pm 212$  ppm), whilst Strombolian glasses contain uniformly low  $S_{MG}$  concentrations (418–640 ppm; average  $490 \pm 82$  ppm; Þórðarson et al., 1996). These residual sulfur concentrations correspond to contrasting degassing efficiencies of 25–70% and 62–75% for hydromagmatic and magmatic activity, respectively, relative to the initial sulfur content of  $1677 \pm 225$  ppm preserved in olivine-hosted melt inclusions ( $S_{MI}$ ; Metrich et al., 1991; Þórðarson et al., 1996).

The progressive exsolution of sulfur with decreasing magma overpressure is well-recorded in exposed subglacial volcanic edifices (tuyas) in Iceland (Moore and Calk, 1991) and elsewhere (e.g., British Columbia; Dixon et al., 2002; Edwards et al., 2009; Hungerford et al., 2014), which exhibit decreasing  $S_{MG}$  with increasing elevation. Glassy hyaloclastite samples erupted at water depths >400 m (equivalent to 4 MPa hydrostatic pressure) contain  $S_{MG} \geq 500$  ppm, whilst the glassy margins of all subaerial lava flow units capping tuyas are degassed to  $S_{MG} \leq 200$  ppm (Moore and Calk, 1991). Similarly, glassy pillow basalt rims erupted under variable water depths off the Reykjanes Ridge (SE Iceland) indicate that sulfur is largely retained in the melt until ~200 m water depth (~2 MPa hydrostatic pressure) after which sulfur degassing takes place rapidly (Moore and Schilling, 1973). The elevated  $S_{MG}$  values observed in hydromagmatic tephra are therefore consistent with higher quench pressures, whereby rapid cooling of magma during MWI arrests degassing and thus preserves the residual melt volatile concentration at the depth of interaction (Þórðarson et al., 1996; Mastin et al., 2004).

Hawaiian basalts exhibit a similar dichotomy in volatile content between magmatic and hydromagmatic tephra, but with the transition displaced to slightly lower S contents than the more iron-rich Icelandic basalts (Moore et al., 1965; Moore and Fabbi 1971; Mastin et al., 2004; Schipper et al., 2010). Tephra from the Keanakākoʻi eruption of Kīlauea (where magma interacted with a surface lake; Mastin et al., 1997) have  $S_{MG}$  between 250 and 600 ppm, which are again elevated relative to those of equivalent ‘dry’ Kīlauean lava fountain deposits (<100–300 ppm; e.g., Swanson and Fabbi, 1973; Mastin et al., 2004; Sides et al., 2014; Moussallam et al., 2016; Helz et al., 2017). Similarly, eruptive products from the submarine (<1400 ppm S) and subaerial (100–200 ppm S) rift zones of Mauna Loa exhibit similarly contrasting volatile contents, with glassy submarine pillow rims also preserving decreasing S and Cl concentrations with reduced water depths (Davis et al., 2003).

In this study, we interrogate volatile data from magmatic and hydromagmatic pyroclasts erupted contemporaneously during the Hverfjall Fires, Iceland, to (a) reconstruct the degassing history of magma erupted under different eruptive styles, (b) determine the magma vesicularity at the time of MWI and quenching, (c) calculate the fragmentation pressure/depth of MWI, and (d) explore how changing conditions of magma ascent and fragmentation may relate to transitions in eruptive behaviour. From these data, we consider sulfur degassing in ocean island basalts (OIB) more generally, and evaluate the use of volatiles as geochemical indicators of hydromagmatic processes.

## **2. Geological setting**

The Hverfjall Fires (~2500 ka) was a major rifting episode within the Krafla Volcanic System, located in Iceland's Northern Volcanic Zone (Fig. 1; Þórarinnsson, 1979; Sæmundsson, 1991; Mattsson and Höskuldsson, 2011; Liu et al., 2017). Effusive activity occurred intermittently along a NNE-SSW aligned fissure, which extended both north and south of the central Krafla

caldera within a graben (Sæmundsson, 1991). Most activity was concentrated at the southernmost tip of the fissure, in Mývatn, where coeval ‘dry’ magmatic and hydromagmatic explosive activity formed part of the Jarðbaðshólar scoria cone complex and Hverfjall tuff ring (and surrounding deposits), respectively. Hydromagmatic activity at the Hverfjall vent was initiated and maintained throughout the eruption by the interaction of magma with groundwater aquifers, with the spatial distribution of magma-water interaction (MWI) determined by the pre-existing hydrological flow regime in the region (Liu et al., 2017).

The hydromagmatic deposits from Hverfjall comprise fine-grained ash fall and massive to finely-stratified base surge units, in addition to the complex proximal stratigraphy within the tuff ring edifice itself (Sæmundsson, 1991; Mattsson and Höskuldsson, 2011). In total, hydromagmatic activity generated approximately  $0.15 \pm 0.02 \text{ km}^3$  of pyroclastic material, of which  $0.08 \pm 0.01 \text{ km}^3$  comprise an extensive fine-grained unconsolidated fall deposit formed during the initial stage of the eruption (Liu et al., 2017). Later eruptive phases were dominated by base surges with runout distances of 3–5 km. Proximal surge exposures show a clear evolution from poorly-sorted matrix-supported massive lapilli-tuff basal units (e.g., H<sub>8.9</sub> A; Fig. 1c, Table 1) through to well-sorted clast-supported accretionary lapilli-rich intermediate and upper units intercalated with thinly-laminated fine ash (e.g., H<sub>8.9</sub> F), suggesting a transition from water-saturated to drier emplacement conditions. Large angular blocks and bombs of dense basaltic lavas indicate considerable disruption of the basement substrate by subsurface explosions, although lithic clasts comprise only a minor proportion of medial to distal ash fall deposits (< 10%; Liu et al., 2017). The presence of lithic material throughout stratigraphic sections indicates continuous country rock excavation (e.g., Lorenz, 1986, 2003) and/or recycling and ejection of earlier disrupted material (Graettinger et al., 2014; Valentine et al., 2015, 2017; Lefebvre et al., 2012, 2016). However, the homogeneous lithology of basement rocks and the potential for progressive upward mixing prior to ejection means that the lithic

assemblage provides little constraint on the absolute depth of disruption (e.g., Agustín-Flores et al., 2014; Valentine et al., 2017).

‘Dry’ magmatic activity occurred from a vent within the Jarðbaðshólar cone complex (located ~3 km north of Hverfjall along the fissure strike), during which predominantly Strombolian activity produced a coarse, scoriaceous deposit (with a more limited dispersal distance of ~1.5 km) and subsequent lava flows (Mattsson and Höskuldsson, 2011; Liu et al., 2017). Interbedded magmatic and hydromagmatic deposits indicate that the Hverfjall and Jarðbaðshólar vents were active simultaneously (Mattsson and Höskuldsson, 2011). However, clear differences in the total grain size distribution (TGSD) of erupted tephra highlight contrasting fragmentation efficiencies at the two vents. Specifically, the opening hydromagmatic fall deposit comprises 97 wt% ash-sized material (<2 mm), of which 20 wt% is fine ash (<63 µm). In contrast, ash-sized material comprises <12% of the total mass of magmatic fall deposits (Liu et al., 2017).

The four deposit types – hydromagmatic fall, hydromagmatic surges, magmatic fall and lava flows – are rarely observed together because of the limited spatial extent of the magmatic units. However, where multiple units are exposed together (e.g., Fig. 1d), stratigraphic relationships suggest that magmatic and hydromagmatic vents were active contemporaneously (Mattsson and Höskuldsson, 2011; Liu et al., 2017). Figure 1d illustrates a representative depositional sequence observed in the field. Although the deposition of hydromagmatic material (pyroclastic fall followed by base surges) appears in many sections to have begun prior to the onset of magmatic fall, the presence of coarse magmatic lapilli directly above the Hekla-3 silicic tephra in sections proximal to Jarðbaðshólar suggest that the two vents may have initiated near-synchronously. Finely-stratified surge deposits overlying magmatic fall and lava flow units, even in proximal locations, indicates that hydromagmatic explosive activity continued at the Hverfjall vent after activity ceased at Jarðbaðshólar (Liu et al., 2017).

Overlapping vesicularity and bubble number density distributions measured in rapidly quenched magmatic and hydromagmatic pyroclasts (from the Hverfjall Fires as well as mafic eruptions more generally) indicate a shared initial history of bubble nucleation and growth, with substantial vesiculation prior to MWI (Mastin et al., 2004; Murtagh and White, 2013; Liu et al., 2017). The elevated fragmentation efficiency of hydromagmatic deposits has been attributed, at least in part, to brittle disintegration of vesicular pyroclasts due to high thermal stress generated during fast cooling (Mastin et al., 2004; Liu et al., 2015, 2017; Van Otterloo et al., 2015), although rapid steam expansion resulting from coarse mixing of magma and water also contributes to fine fragmentation by molten fuel coolant interaction (Wohletz, 1986; Zimanowski et al., 1991, 1997).

### 3. Material and methods

Fieldwork and sampling locations are described in detail in Liu et al. (2017); the subset of samples used in this study is listed in Table 1. Unconsolidated tephra samples were dried, sieved in phi ( $\phi$ ) intervals, and size fractions between  $-1\phi$  (2–4 mm) and  $4\phi$  (64–125  $\mu\text{m}$ ) mounted in polished grain mounts. Thin sections were made through two 16–32 mm lapilli (from Jarðbaðshólar) that exhibit clear quenched rims, and through consolidated surge deposit samples comprising a range of grain sizes from  $-2\phi$  (4–8 mm) to fine ash ( $<64 \mu\text{m}$ ). No large lapilli  $> 8$  mm were found in the unconsolidated hydromagmatic tephra deposits (Liu et al., 2017).

Major element and dissolved sulfur (S) and chlorine (Cl) concentrations of matrix glass and olivine- and plagioclase-hosted melt inclusions (MI) were measured on carbon-coated polished grain mounts using the JEOL 8530F Field Emission Gun electron microprobe (FEG-EPMA) at the University of Bristol, UK. Analyses were performed under operating conditions of 20 kV accelerating voltage and 40 nA beam current, using a defocused beam (10  $\mu\text{m}$ ) to

minimise sodium mobility. A combination of mineral and glass standards were used for calibration. Repeat analyses of Smithsonian basaltic glass reference materials yielded average values of  $1395 \pm 38$  [1 $\sigma$ ] ppm S (VG2, Juan de Fuca Ridge, NMNH 111240-52) and  $168 \pm 35$  [1 $\sigma$ ] ppm S (VGA-99, Mahaopuhi lava lake, Hawai'i, NMNH 113498-1), and established that no instrumental drift corrections were needed. Counting times for each element were 10 s for Na, Si, Al, K and Ca, 30 s for Mg and Fe, 40 s for P, 60 s for Mn, and 120 s for S and Cl, over a total analysis time of 120 s. Detection limits were 26 ppm (S) and 16 ppm (Cl) under the chosen operating conditions. The oxidation state of sulfur in matrix glass (magmatic and hydromagmatic) was determined from the wavelength of the S  $k\alpha$  peak, according to the method of Carroll and Rutherford (1988; see Appendix A for full details).

To back-calculate liquid lines of descent, reverse fractional crystallisation models were initiated using the average hydromagmatic glass composition and isobaric crystallisation pressures of 0.001, 2, 4, and 6 kbar. Calculations were performed at the FMQ oxygen fugacity buffer using the mineral-melt equilibrium models of Danyushevsky (2001) for olivine, plagioclase and clinopyroxene and with  $Kd_{Fe-Mg}^{ol-liq}$  modelled after Toplis (2005). Criteria for the exclusion of mineral phases from the crystallising assemblage were Fo > 92 mol% (olivine), An > 92 mol% (plagioclase), and Mg# > 90 (clinopyroxene).

H<sub>2</sub>O and CO<sub>2</sub> concentrations in matrix glasses were determined by Fourier Transform Infrared Spectroscopy (FTIR) at the University of Bristol, UK. FTIR spectra were measured on doubly-polished glass wafers, with between 2 and 5 spot analyses per sample (Table S2, supplementary information). The window size was kept constant at 100×100  $\mu\text{m}^2$  for all hydromagmatic wafers (except one at 75×75  $\mu\text{m}^2$ ). Peak heights (absorbances) at 3550  $\text{cm}^{-1}$  [H<sub>2</sub>O] and 1520 and 1430  $\text{cm}^{-1}$  [CO<sub>3</sub><sup>2-</sup> doublet] were measured using a linear baseline, and converted to absolute concentrations using the Beer Lambert Law,  $c = \frac{MA_\lambda}{\rho d \epsilon}$ , where  $M$  is the

9  
molecular weight of H<sub>2</sub>O or CO<sub>2</sub>,  $A$  is the measured absorbance at the band of interest ( $\lambda$ ),  $\rho$  is

the density of the basalt glass [ $2.76 \text{ g cm}^{-3}$ ],  $d$  is the thickness of the glass wafer, and  $\epsilon$  is the molar absorption coefficient ( $\text{H}_2\text{O}$ :  $63 \text{ L mol}^{-1} \text{ cm}^{-1}$ ; Dixon et al., 1995;  $\text{CO}_2$ :  $375 \text{ L mol}^{-1} \text{ cm}^{-1}$ ; Fine and Stolper, 1986). Sample thicknesses were measured to a precision of  $\sim 3 \text{ }\mu\text{m}$  using a micrometer, and ranged from 38 to  $148 \text{ }\mu\text{m}$ .

#### 4. Results

Ash particles from both hydromagmatic and magmatic deposits are mostly glassy sideromelane, with phenocrysts of plagioclase, clinopyroxene, and olivine, in order of decreasing abundance (Fig. 2a). Phenocrysts are present either as individual crystals or, more commonly, within two- or three-phase glomerocrysts, and contain rare small melt inclusions (MIs). Fe-Cu-Ni sulfide globules ( $< 1\text{--}30 \text{ }\mu\text{m}$  in diameter) are often found within the interstitial glass/MIs of glomerocrysts and free phenocrysts, and, less frequently, in the matrix glass (Fig. 2b).

Matrix glasses are tholeiitic basalt in composition, containing  $50.6 \pm 0.2 [1\sigma] \text{ wt\% SiO}_2$  and  $5.68 \pm 0.13 [1\sigma] \text{ wt\% MgO}$  (Table S1, supplementary information). Magmatic glasses (from Jarðbaðshólar) are compositionally similar to hydromagmatic glasses (from Hverfjall), but are very slightly more primitive (higher MgO content) and lie along modelled reverse fractional crystallisation paths from the average hydromagmatic composition (Fig. 3b-d). Melt inclusions (MIs) trapped within olivine and plagioclase phenocrysts have major element compositions that are near-indistinguishable from the surrounding matrix glass, indicating melt isolation during a very late-stage of fractional crystallisation (Fig. 3). Close compositional agreement between olivine- and plagioclase-hosted inclusions, particularly in diagnostic elements such as Fe, Ca and Al, suggest negligible post-entrapment modification due to host crystallisation (no corrections have been applied). Many of the phenocrysts that host MIs

(particularly olivine) have partially to fully skeletal morphologies, suggesting rapid crystal growth (Fig. 2c).

The dissolved sulfur concentration preserved in matrix glass ( $S_{MG}$ ) represents the residual sulfur remaining in the melt at the time of quenching. Quenching refers to the rapid cooling of melt to below the glass transition temperature, where the diffusivity of a volatile phase (such as S) becomes sufficiently slow that the melt concentration becomes essentially static on the timescales of interest. Figure 4 shows a clear offset in the distributions of  $S_{MG}$  between hydromagmatic (Hverfjall) and magmatic (Jarðbaðshólar) deposits.  $S_{MG}$  in magmatic ash varies between 200 and 500 ppm (average:  $418 \pm 93$  [1 $\sigma$ ] ppm).  $S_{MG}$  is elevated within hydromagmatic ash, and spans a much larger range, from 550 to 1450 ppm (average:  $883 \pm 172$  [1 $\sigma$ ] ppm). MIs preserved in all mineral phases record dissolved sulfur concentrations,  $S_{MI} = 1400\text{--}1700$  ppm (average:  $1522 \pm 127$  [1 $\sigma$ ] ppm) and chlorine concentrations,  $Cl_{MI} = 145\text{--}200$  ppm (average:  $165 \pm 27$  [1 $\sigma$ ] ppm; Figs. 4, 5 black crosses; Table S1, supplementary information). Assuming MIs were trapped prior to the onset of low pressure S or Cl degassing,  $S_{MI}$  and  $Cl_{MI}$  represent the maximum S and Cl contents of the magma at higher pressures. The most undegassed hydromagmatic glasses have sulfur concentrations that overlap those of co-erupted phenocryst-hosted melt inclusions. Cl concentrations in both magmatic and hydromagmatic matrix glasses ( $Cl_{MG}$ ) are also generally indistinguishable from those of melt inclusions (Fig. 5), although the range of  $Cl_{MG}$  in magmatic samples extends to lower values ( $\sim 110$  ppm), indicating partial loss.

To test the relationship between macroscopic evidence of degassing (vesicles) and preserved volatile concentrations, we classified each compositionally analysed grain into one of three classes – dense, vesicular, or bubble shard – depending on its vesicularity and morphology, following the criteria defined by Liu et al., (2017). We find no clear correlation between the measured  $S_{MG}$  and the particle vesicularity within individual samples: dense glass



fragments, vesicular particles, and bubble shards show the same range of sulfur concentrations (Fig. 4). Temporally, a stratigraphic sequence through the surge deposits (site 8.9 A–F, where A refers to the basal sample; Fig. 4) suggests a slight shift towards higher  $S_{MG}$ , concurrent with a sedimentological transition from poorly-sorted matrix-supported lapilli-tuff (A) to well-sorted clast-supported alternations of fine ash and accretionary lapilli (C–F).

Lapilli from Jarðbaðshólar cone deposits ( $M_{Q1}$ ) exhibit marked cross-sectional variations in vesicle texture. Whilst clast rims typically preserve small spherical vesicles within a glassy matrix (although with noticeable heterogeneity in spatial distribution), cores are highly vesicular with large, irregularly-shaped vesicles that are often interconnected and record expansion, coalescence and deformation. The transition between the two textural regions is often abrupt. Interstitial glass within clast cores is frequently finely microcrystalline, although regions of sideromelane can still be identified. These variations in vesicularity and vesicle morphology are accompanied by a similarly abrupt decrease in  $S_{MG}$  from rim to core, coincident with the sharp textural boundary (Fig. 6; Table S1, supplementary information). Measured profiles on three clasts show that while sulfur concentrations in the outermost (quenched) clast rim lie between 375 and 500 ppm, concentrations in the centre of the same clasts along a near-linear core to rim profile are typically 200–350 ppm and exhibit more marked local heterogeneity.

$H_2O$  concentrations in hydromagmatic matrix glasses from the basal fall deposit range from 0.40 to 0.51 wt%, with an average of  $0.45 \pm 0.03$  [ $1\sigma$ ] wt% (Fig. 7; Table S2, supplementary information). Scatter in the measured concentrations increases with decreasing polished sample thickness (Fig. S1, supplementary information), and the thickest glass wafers ( $>100 \mu m$ ) yield an average  $H_2O$  concentration of  $0.43 \pm 0.016$  [ $1\sigma$ ] wt%. Dissolved water is present only in the form of hydroxyl ( $OH^-$ ), with no detection of a molecular water peak at  $1630 \text{ cm}^{-1}$ . This result agrees with previous FTIR studies of basaltic glass showing that at low

dissolved water contents ( $<0.5$  wt%) hydroxyl groups are the only detectable hydrogen-bearing species (Stolper et al., 1982; Dixon et al., 1988), and provides evidence that the water is magmatic in origin.  $\text{CO}_2$  is below detection ( $< \sim 4$  ppm) in most samples, but is measurable at 14–19 ppm in four of the thickest sample wafers ( $>100$   $\mu\text{m}$ ). Magmatic matrix glasses contain much lower  $\text{H}_2\text{O}$  concentrations of  $0.12 \pm 0.48$  [1 $\sigma$ ] wt%, with  $\text{CO}_2$  below detection in all samples (Fig. 7).

Sulfur species in matrix glasses from the Hverfjall Fires tephra are sulfide-dominated (Fig. S2; Table S3, supplementary information), with  $\text{S}^{6+}/\text{S}_{\text{total}}$  ranging from  $<0.11$  (hydromagmatic) and 0.04 to 0.49 (magmatic). The results are independent of the dwell time used in the analytical procedure (Appendix A, supplementary information). Using the XANES calibration of Jugo et al., (2010), measured sulfur speciation ratios yield average oxygen fugacities of  $\text{FMQ} + 0.4 \pm 0.17$  (1 $\sigma$ ; hydromagmatic) and  $\text{FMQ} + 0.6 \pm 0.33$  (1 $\sigma$ ; magmatic).

## 5. Discussion

### 5.1 Reconstructing the degassing processes

Volatile concentrations in erupted tephra provide valuable insights into the pressure/depth and timing (relative to the onset of magmatic vesiculation) of magma-water interaction, particularly when interpreted in the context of clast textures. Taking the highest  $\text{S}_{\text{MI}}$  value to represent the maximum pre-degassing sulfur concentration in the melt, the range of sulfur contents retained within hydromagmatic matrix glasses indicate that the magma had lost between 17 and 70% of its initial sulfur prior to quenching. This result demonstrates that the magma was already vesiculating at the time of MWI, consistent with previous interpretations based on clast textures and morphologies in this (Liu et al., 2017) and other hydromagmatic eruptions (e.g., Capelas tuff cone, Azores [shallow marine], Mattsson, 2010; Keanakāko'i, Hawai'i [shallow sublacustrine], Mastin et al., 2004; Askja, Iceland [subglacial], Graettinger et al., 2013).

Magmatic matrix glasses record substantially lower residual volatiles (70–83% degassed) than hydromagmatic tephra of equivalent size, despite sharing near-identical initial melt volatile concentrations (from MIs; Fig. 4) and overlapping oxidation states (from S speciation; Fig. S2). This dichotomy indicates near-surface divergence in degassing processes between hydromagmatic and magmatic vents, and could be accounted for by several potential mechanisms, including (a) post-fragmentation degassing; (b) kinetic fractionation; or (c) differences in the quench pressure (depth). Distinguishing the dominant mechanism has implications for our understanding of the respective environments and mechanisms of fragmentation (Wallace and Edmonds, 2011; Wallace et al., 2015).

Fragmentation and quenching are not always contemporaneous. Volatile losses following primary fragmentation depend on the time for individual clasts to cool to below the glass transition interval,  $T_g$ , which is in turn controlled by clast size and cooling rate (Dingwell and Webb, 1989; Lloyd et al., 2013). Importantly, the analyses shown in Figures 4 and 5 are from ash-sized particles <1 mm in diameter (unless stated), for which whole-clast cooling timescales are rapid (< 0.1 s, based on simple conductive models; Porritt et al., 2012; Helo et al., 2013). Indeed, fast cooling rates of  $10^{3.7} - 10^{5.1} \text{ K s}^{-1}$  have been determined for angular submarine hyaloclastite fragments 0.5–1 mm in diameter (Helo et al., 2013). Moreover,  $S_{MG}$  is independent of particle size in the range 0.06 to 4 mm (and the quenched rims of 16–32 mm magmatic lapilli; Fig. S3, supplementary information; note that no hydromagmatic lapilli of this grain size were found for comparison), and thus does not appear to be determined by cooling-rate. The cooling timescale for the cores of larger magmatic clasts is more protracted, however. Brittle surface cracks on many coarse lapilli and bombs indicate that the interior of the clasts remained hot enough to accommodate continued degassing and bubble expansion after the clast exterior had already cooled to below  $T_g$  (Wright et al., 2007; Porritt et al., 2012). Co-variation in  $S_{MG}$  and vesicle texture in core-to-rim profiles of magmatic lapilli (16–32 mm

diameter) provides geochemical evidence for extensive post-fragmentation degassing of clast interiors (Fig. 6). Partial Cl degassing of some magmatic matrix glasses also reflects shallow post-fragmentation volatile losses, as Cl is soluble to low pressures in basaltic melts (Fig. 5). Importantly, however,  $S_{MG}$  values in both rapidly-quenched lapilli rims and in ash-sized particles from the Jarðbaðshólar scoria cones are still lower than in the most degassed hydromagmatic matrix glasses from Hverfjall. Post-fragmentation degassing can therefore account for the range of 200–500 ppm S in magmatic matrix glasses, but an alternative process is required to fully explain the difference in final volatile concentrations between magmatic and hydromagmatic tephra.

Under conditions of disequilibrium degassing, where the magma ascent rate is faster than the timescale required for volatile species to diffuse into bubbles, volatile concentrations in matrix glasses are determined by the relative diffusivities of each component (kinetic fractionation) rather than by their respective solubilities. Sulfur has a low diffusivity relative to  $H_2O$ , which diffuses very rapidly in basaltic melts (Freda et al., 2005; Zhang and Stolper, 1991), and would therefore be preferentially elevated relative to  $H_2O$  in melt that had experienced disequilibrium degassing. Hydromagmatic matrix glasses are elevated in both S and  $H_2O$  compared to magmatic tephra of equivalent size (Fig. 7), suggesting that the difference in residual sulfur content cannot be explained entirely by kinetic fractionation. However, without corresponding measurements of initial  $H_2O$  concentrations (e.g., from melt inclusions) or quantitative determinations of volatile diffusivities at the relevant conditions, disequilibrium degassing cannot be ruled out entirely and indeed may have contributed to the observed variability in  $S_{MG}$ .

Volatile solubilities and fluid-melt partition coefficients are strongly pressure-dependent (e.g., Dixon et al., 1997; Newman and Lowernstern, 2002; Moretti et al., 2003; Papale et al., 2006; Witham et al., 2012; Wallace et al., 2015; Edmonds and Wallace, 2017).

Under conditions of equilibrium degassing, and assuming no post-fragmentation losses, elevated volatile concentrations at the time of quenching are consistent with a higher saturation pressure ( $P_{sat}$ ). Calculated H<sub>2</sub>O-CO<sub>2</sub> saturation pressures, using the VolatileCalc thermodynamic model of Newman and Lowenstern (2002), are 1.6–2.6 MPa for Hverfjall hydromagmatic glasses, with an average of  $2.1 \pm 0.3$  [1 $\sigma$ ] MPa, if we assume conservatively that CO<sub>2</sub> is present at 0 ppm when below the FTIR detection limit. To evaluate the uncertainty in saturation pressures introduced by variation in CO<sub>2</sub> below the FTIR detection limit, we repeat the calculations taking CO<sub>2</sub> to be present at either 5 or 20 ppm; these calculations yield higher average pressures of  $3.2 \pm 0.3$  or  $6.5 \pm 0.3$  [1 $\sigma$ ] MPa, respectively. Thus, for a given H<sub>2</sub>O content, saturation pressures are extremely sensitive to the CO<sub>2</sub> content, such that varying CO<sub>2</sub> between 0 and 20 ppm produces a ~4 MPa change in  $P_{sat}$ , whilst variation in H<sub>2</sub>O over the measured range of 0.40–0.51 wt% accounts for only 1 MPa change.

Closed-system degassing paths calculated using the SolEx multi-phase C-O-H-S model with full compositional parameterisation (Fig. 8; Witham et al., 2012) indicate a similar, but slightly higher, range of saturation pressures of 2.2–7.0 MPa for Hverfjall hydromagmatic glasses (initiated using the average melt composition from Table S1, and initial volatile concentrations of 1.2 wt% CO<sub>2</sub>, 0.6 wt% H<sub>2</sub>O, 1500 ppm S, and 160 ppm Cl; Neave et al., 2014; Hartley et al., 2014). Oxygen fugacity was fixed at the minimum value of NNO=0.5. Calculated H<sub>2</sub>O-CO<sub>2</sub> saturation pressures obtained using either model are independent of temperature over the tested range of 1000–1150°C.

In contrast, the lower volatile contents of magmatic glasses from Jarðbaðshólar suggest the erupted melt was degassing to near 1 atm with respect to H<sub>2</sub>O and CO<sub>2</sub> (Fig. 7). Continued post-fragmentation degassing of S and Cl in magmatic tephra, however, demonstrates that not all volatile components had fully equilibrated to atmospheric conditions at the time of fragmentation.

Differences in the relative confining pressure at the time of fragmentation and quenching could produce the contrasting residual volatile abundances in magmatic and hydromagmatic glasses. Note that the hydromagmatic glasses analysed for both S and H<sub>2</sub>O are at the upper end of the range of S<sub>MG</sub> measured at Hverfjall (dense sideromelane grains were preferentially selected), suggesting that the calculated saturation pressures are upper bounds. The total range of S<sub>MG</sub> concentrations (550–1450 ppm) records quenching over a large pressure interval, from <2.6 MPa (or <6 MPa if uncertainty in CO<sub>2</sub> below the detection limit is considered) to near-atmospheric conditions. Calculated degassing paths indicate that H<sub>2</sub>O does not begin to degas significantly from the melt until <6 MPa (Fig. 8), thus implying that the Hverfjall magma underwent a rapid burst of vesiculation in the uppermost few hundred metres of ascent. Interestingly, the SolEx solubility model, initiated using the Hverfjall Fires magma composition, predicts that sulfur would begin to partition into a fluid phase at ~40–50 MPa (far earlier than H<sub>2</sub>O) and have degassed 95% of its initial sulfur by 16 MPa (Fig. 8). This result is in poor agreement with our measured degassing efficiencies, which suggest up to 90% of the initial sulfur is retained until <6 MPa. This discrepancy between measured and modelled sulfur contents could indicate that sulfur is degassing under a conditions of significant disequilibrium. However, S and Cl fluid-melt partitioning in SolEx is calibrated based on more oxidised, hydrous basaltic melts ( $\Delta\text{NNO} = +1.6 - +2.1$ , >3 wt% H<sub>2</sub>O; Lesne et al., 2011; Witham et al., 2012) than either Hverfjall or Kīlauea (Moussallam et al., 2016; Helz et al., 2017), in which sulfur will be present largely in the form of S<sup>6+</sup> and H<sub>2</sub>O will begin to exsolve at higher pressure. Sulfur solubility in basaltic melts is strongly dependent on  $f\text{O}_2$  (see Section 4.2), and further experimental and petrological work is needed to calibrate thermodynamic models for sulfur degassing in reduced basaltic magmas.

## 5.2 Was the Hverfjall Fires magma sulfide-saturated?

Dissolved sulfur concentrations in reduced basaltic melts [ $S^{2-}$ ] are buffered by the stability of immiscible Fe-S-O (sulfide) phases (Edmonds and Mather, 2017). Sulfur solubility is also strongly coupled to the melt FeO content as  $S^{2-}$  dissolves primarily by complexing with  $Fe^{2+}$  (Mathez, 1976; Wallace and Carmichael, 1992; O'Neill and Mavrogenes, 2002; Liu et al., 2007, Moretti and Baker, 2008), such that Fe-rich magmas can dissolve greater amounts of sulfur before reaching sulfide saturation compared to Fe-poor magmas (Wallace and Carmichael, 1992). For the Hverfjall Fires matrix glass composition ( $14.6 \pm 0.16$  [1 $\sigma$ ] wt% FeO), the theoretical sulfur content at sulfide saturation (SCSS) is ~1800 ppm (Wallace and Carmichael, 1992; Mavrogenes and O'Neill, 1999; Wallace and Edmonds, 2011), which is in good agreement with the maximum sulfur concentration measured in melt inclusions (1737 ppm). Together with the presence of metastable Fe-Cu-Ni sulfide globules in erupted tephra (Fig. 2b), the sulfur concentrations of melt inclusions and the least degassed matrix glasses suggest that the parent magma was at, or close to, sulfide saturation throughout crystallisation and magma ascent. Late-stage degassing, in contrast, drives oxidation and progressive resorption of sulfides (Patten et al., 2013; Edmonds and Mather, 2017).

### **5.3 Depth of magma-water interaction during the Hverfjall Fires**

Combined with additional  $H_2O$  and  $CO_2$  measurements, our sulfur dataset places quantitative constraints on the pressures recorded by melt quenching. If quenching and fragmentation are taken to be contemporaneous during MWI (e.g. Liu et al., 2015, 2017), calculated quench pressures reflect the depth of fragmentation. This pressure-to-depth conversion requires us to consider the most appropriate pressure gradient. For the case of hydrostatic pressure, saturation pressures of 1.6–2.6 MPa (VolatileCalc) translate to fragmentation depths of 158–258 m, with an average of  $210 \pm 30$  m. However, assuming lithostatic pressure and taking the density of the overlying country rock to be  $\sim 2.76$  g cm $^{-3}$  (dense basaltic lava flows), measured saturation

pressures translate to shallower fragmentation depths of 57–94 m, with an average of  $74 \pm 11$  m (Fig. 9). It is worth re-emphasising that  $P_{sat}$  is highly sensitive to CO<sub>2</sub>, particularly at the low pressures of interest; therefore, the upper bound of saturation pressures may extend as high as ~6 MPa (20 ppm CO<sub>2</sub>) due to uncertainty in the absolute CO<sub>2</sub> concentration below the FTIR detection limit.

Interestingly, the depth distribution for lithostatic pressure is consistent with experimentally-determined optimum explosion depths of ~100 m, and maximum depths for subaerial tephra ejection of ~200 m (Graettinger et al., 2014; Valentine et al., 2014). Similar explosion depths of 30–115 m were derived for large blocks found in ejecta within natural deposits, assuming near-optimal scaled depths ( $0.004 \text{ m/J}^{1/3}$ ) and explosion energies determined from the deposit volume and calculated ejection velocities (Graettinger and Valentine, 2017). Notably, these depth estimates are sensitive to both assumptions made during the calculation of ejection velocities and uncertainties on the mass ejected, and so the observed ejecta could easily reflect deeper source locations by 10s of metres (Graettinger and Valentine, 2017), thus potentially improving further the correspondence with the saturation pressures calculated here. However, dissolved volatile concentrations remain elevated throughout the eruption stratigraphy (Fig. 4), and it is difficult to envisage how lithostatic pressure (or close to) could be maintained throughout the eruption after vent opening.

Alternatively, an in-vent water-saturated sediment slurry, comprising variable amounts of external water, lithic material and juvenile recycled tephra (Kokelaar, 1986; White, 1996, Schipper and White, 2016), would have a density intermediate between pure water and country rock, and the volatile saturation pressures in quenched glass would therefore correspond to fragmentation depths intermediate between lithostatic and hydrostatic end-members. The presence of recycled clasts within coarse ash and lapilli from Hverfjall (Fig. 2d; Liu et al., 2017) supports the magma-slurry hypothesis, as does the broad range of  $S_{MG}$  measured in



hydromagmatic pyroclasts (Figs. 4, 10). The substantial variations in confining pressure implied by the large range of  $S_{MG}$  may record temporal or spatial variations in the water-sediment proportions within the slurry and the thickness of the slurry layer itself, without the need to invoke fragmentation over a large depth interval. Local pressure fluctuations resulting from discrete explosions (implied by the repeating sequences of lapilli-ash graded couplets in proximal deposits; Liu et al., 2017; Graettinger and Valentine, 2017) may also introduce transient departures from a linear depth-pressure relationship, thus contributing further to the variability in  $S_{MG}$ . During periods of high magma supply, pyroclasts in the centre of the uprush column may have been thermally insulated and experienced minimal MWI, consistent with observations of incandescence in the eruption column during continuous uprush phases at Surtsey (Pórarinnsson, 1967) and Capelinhos (Cole et al., 2001). In this case, the depth of quenching may be significantly shallower than that of fragmentation. Further, as a result of clast recycling within the vent slurry, sampled clasts may represent time-averaged conditions over an interval longer than the deposition of an individual bed. Time-averaging in this way may contribute to the apparent geochemical homogeneity (Houghton and Smith, 1993; Graettinger et al., 2016; Schipper and White, 2016).

In the context of the regional hydrology, our geochemical data are consistent with interaction with a groundwater aquifer (Liu et al., 2017), with the development of an in-vent slurry maintaining and modulating confining pressures after vent opening. The opening phase of hydromagmatic activity generated a widespread tephra fall deposit prior to the onset of surge emplacement (Mattsson and Höskuldsson, 2011). Although vertical migration of the locus of MWI could have contributed to this change in eruption style (Graettinger et al., 2014, 2015; Valentine et al., 2014), the range of  $S_{MG}$  remains relatively constant between hydromagmatic fall and base surge deposits, suggesting that pyroclasts were quenched under a similar range of pressure conditions and arguing against significant migration of the fragmentation surface.

However, we cannot exclude small-scale migration on the scale of metres to tens of metres, as this would not be resolvable with our volatile data. In-vent recycling of pyroclasts may also have contributed to the homogenisation of subtle temporal trends. Alternatively, the transition from fall- to surge- dominated deposition may record a reduction in the volumetric magma flux, and thus a change in the magma-water mixing ratio and resultant energy transfer (Mattsson and Höskuldsson, 2011) or to variations in the vent geometry (e.g., cone growth).

Interestingly, the data shown in Figure 4 suggest a subtle increase in  $S_{MG}$  during the transition from ‘wet’ to ‘dry’ surges (inferred from sedimentological properties of the deposits; Liu et al., 2017). This increase in  $S_{MG}$  through time cannot be explained by progressive degassing of a single magma batch, which would gradually deplete sulfur in the melt. Instead, this increase may reflect either elevated confining pressure (associated with the establishment of, or changing conditions within, an in-vent magma-slurry), or small-scale (10s of metres) migration of the fragmentation level, which has been shown to influence deposition processes (Grättinger et al. 2015). Explosions beneath the centre of a pre-existing crater that occur deeper than their optimal scaled depth, form narrow debris jets that mainly collapse back into the crater (Taddeucci et al. 2013; Grättinger et al. 2014, 2015). The collapse results in the lateral displacement of gas and particles, generating dilute fine-grained density currents. These dilute flows produce fine-grained stratified and cross-stratified deposits, which closely resemble the stratified tuffs resulting from ‘dry’ base surges in natural systems (e.g., Waters & Fisher, 1971; Chough & Sohn 1990; Valentine et al. 2015).

The major element glass compositions of the crater samples ( $H_{5.11}$ ) are indistinguishable from the surrounding fall and surge deposits (Fig. 3), supporting a genetic link. Nevertheless, large uncertainties remain regarding timing of edifice growth relative to the emplacement of these distal deposits. Figure 4 shows that the crater samples are slightly

elevated in  $S_{MG}$  relative to initial fall deposits and are instead more similar to the late-stage surges ( $H_{8.9}$  C–F).

#### **5.4 Sulfur degassing in ocean island basalts**

Figure 10a synthesises sulfur data in matrix glasses and melt inclusions from a range of basaltic volcanic systems in Iceland. The compilation includes tephra from hydromagmatic environments that include subglacial (e.g., Grímsvötn, Katla; Óladóttir et al., 2008; Sigmarsson et al., 2013; Liu et al., 2015), shallow seawater (e.g., Surtsey; Schipper et al., 2015), and surface/subsurface groundwater interactions (e.g., Laki; Þórðarson et al., 1996). Hydromagmatic matrix glasses span a broad range in sulfur content from 1500 to 600 ppm. Tephra produced during purely magmatic phases, in contrast, consistently contain  $<600$  ppm residual  $S_{MG}$  (Þórðarson et al., 1996; 2003). Co-erupted lavas typically retain  $S_{MG} < 100$  ppm, indicating further degassing during flow emplacement (Þórðarson et al., 1996).

Vapour-saturation in reduced ocean island basalts, particularly with respect to  $H_2O$ , occurs late and shallow relative to hydrous arc basalts (Gerlach, 1986; Dixon et al., 1991; Wallace and Edmonds, 2011; Edmonds and Wallace, 2017), the result is a burst of vesiculation at depths of only a few hundred metres beneath the ground surface. Significant sulfur loss through fluid-melt partitioning into a vapour phase is therefore delayed until melts become water-saturated. Figure 11 shows how vesicularity (considering here only  $H_2O$  exsolution) varies as a function of pressure for mafic melts at  $1125^\circ\text{C}$ , for different initial water concentrations. For an initial  $H_2O$  concentration of 0.5 wt% (close to the assumed initial Hverfjall concentration of 0.6 wt%), the vesicularity range of 0% (dense fragments) to ~75% (highly vesicular grains) measured in hydromagmatic pyroclasts (Liu et al., 2017; blue shaded region on Fig. 11) can be accounted for by quenching over a pressure range of ~1.5–4 MPa.

This pressure interval agrees well with the range of independent volatile saturation pressures (matrix glass) determined here for the same deposit (grey shaded region on Fig. 11).

Bubble nucleation and growth would not only reduce the material strength of the magma, thereby enabling brittle fragmentation at lower applied stresses (Wagh et al., 1993; Van Otterloo et al. 2015), but may also determine the grain size distribution of fragmented pyroclasts (Liu et al., 2015, 2017). Furthermore, if rapid late-stage volatile exsolution was sufficient to drive magmatic fragmentation, either prior to or synchronous with MWI, then the resulting increase in magma surface area would likely have enhanced the efficiency of magma-water mixing and heat exchange. An interesting consideration is whether vesiculation is a necessary criterion for efficient mixing between magma and water, and therefore for sustained energetic MWI (Houghton et al., 2015).

## 5. Summary and conclusions

Dissolved volatile concentrations in magmatic and hydromagmatic tephra erupted contemporaneously during the Hverfjall Fires provide important constraints on the depth and timing (relative to the onset of magmatic vesiculation) of magma-water interaction (MWI). The magma erupted at both Hverfjall and Jarðbaðshólar vents shared the same magmatic history during dike propagation and decompression to  $\sim 1.6\text{--}2.6$  MPa (average =  $2.1 \pm 0.3$  MPa, which translates to 74 m or 210 m depth assuming lithostatic or hydrostatic pressure, respectively), at which point the Hverfjall magma was quenched by interaction with a system of groundwater aquifers. In contrast, the Jarðbaðshólar magma continued to degas until fragmenting at near-atmospheric pressure followed by late-stage expansion above the vent. This range of pressures/depths for MWI agrees well with those determined from scaled analogue experiments, which suggest that, for a realistic range of energies, only subsurface explosions <200 m depth are likely to breach the surface while those occurring <100 m contribute most to

proximal–medial tephra ring deposits (Taddeucci et al. 2013; Grättinger et al. 2014, 2015; Valentine et al. 2014). That these two independent approaches are converging towards a similar estimate, at least within the bounds of uncertainty, is a very promising result.

Vesicle textures in rapidly quenched hydromagmatic tephra indicate that the magma had already begun to vesiculate prior to magma-water interaction (i.e. >2–6 MPa), where degassing models suggest the vapour phase would have been mostly CO<sub>2</sub>. Sulfur remained dissolved in the melt (or in sulfide phases) until shallow pressures (~2 MPa) concomitant with late-stage H<sub>2</sub>O saturation (and the onset of magmatic fragmentation?). Hydromagmatic matrix glasses record elevated sulfur contents (550–1450 ppm) that reflect degassing of 17–70% of the initial pre-eruptive sulfur in the melt. We attribute this heterogeneity in S<sub>MG</sub> to spatial variations in syn-eruptive magma-water mixing efficiency (manifest as differences in quench rate) and/or to local variations in the effective confining pressure. Such a scenario is consistent with existing models of magma-groundwater interaction in which MWI occurs within an in-vent fluidised slurry comprising a water-saturated mixture of juvenile/recycled pyroclastic and lithic debris (e.g. Hopi Buttes maar-diatreme, US; White, 1991; Surtsey tuff cone, Iceland; Kokelaar, 1983, 1986; White, 1996; Schipper and White, 2016). Slurry formation provides a mechanism through which the elevated confining pressures required by the volatile data could be maintained and buffered throughout the eruption, whilst enabling vertical mixing and ejection of fragmented juvenile and lithic material from a range of depths consistent with emerging models based on experimental and natural explosion data (Graettinger et al., 2014, 2015; Valentine et al., 2014, Graettinger and Valentine, 2017). Furthermore, local variations in confining pressure implied by the large ranges of S<sub>MG</sub> might be easily envisioned within a slurry environment as a result of changes in density (water-sediment proportions), slurry thickness, or pore pressure. Pressure fluctuations from explosions may also contribute to variable confining pressure. From a mixing perspective, the higher viscosity of a slurry relative

to water may enhance the efficiency of magma-water interaction, as the reduced viscosity contrast with the magma would facilitate mingling.

Although elevated throughout, the range of sulfur concentrations in hydromagmatic matrix glass remains relatively constant throughout the eruptive stratigraphy regardless of the eruptive style (i.e. fall- versus surge-dominated deposition). If volatile saturation pressure is taken as a proxy for fragmentation depth, these data imply that the water supply was sufficient to maintain MWI throughout the eruption with no significant vertical migration in the depth of interaction with time (although small-scale migration on the order of metres or tens of metres cannot be excluded). Together with existing constraints on the previous extent of proto-Lake Mývatn (Einarsson, 1982), this stability provides further evidence for magma-groundwater interaction, rather than an eruption through a surface lake where water availability would have been finite (Liu et al., 2017). However, we note that pyroclast recycling within a vent slurry may have contributed to the homogenisation of temporal variability.

To conclude, our results support previous studies (e.g., Davis et al., 2003; Mastin et al., 2004; Schipper et al., 2010a,b; 2011; Hungerford et al., 2014) that show measurements of dissolved volatiles in matrix glass and melt inclusions provide an effective approach to determine (1) the environment of MWI (e.g., groundwater versus surface water, vertical migration of the fragmentation level) and (2) the state of the magma at the time of fragmentation, both critical variables controlling the resulting eruptive style. Together, sulfur and H<sub>2</sub>O contents are sensitive indicators of hydromagmatic processes, particularly for reduced Ocean Island Basalts, as late-stage volatile saturation and degassing (S, H<sub>2</sub>O) occurs at sufficiently low pressures to overlap with typical MWI environments. Although the absolute constraints on  $P_{sat}$  presented here are based on H<sub>2</sub>O contents, S provides an effective indication of relative changes that can be easily measured on larger sample sizes (by EPMA) than is typically achievable for H<sub>2</sub>O (by FTIR).<sup>2</sup> In response to increasing awareness that

morphological and textural pyroclast properties traditionally considered ‘diagnostic’ of MWI are non-unique indicators of fragmentation mechanisms (White and Valentine, 2016; Liu et al., 2017), we emphasise that the dissolved volatile concentrations in matrix glass provide alternative (or additional) properties by which to distinguish magmatic from hydromagmatic eruptive deposits.

## **Acknowledgements**

This work was completed with support for KVC from the AXA Research Fund and a Royal Society Wolfson Merit Award, a Royal Society URF to ACR, and a University of Bristol postgraduate Scholarship to EJJ. Fieldwork was supported by a New Researchers Award from the Geologists’ Association to EJJ. We thank S. Kearns and B. Buse for their assistance with SEM analysis.

## **Figure Captions**

**Figure 1:** Sample locations and field sampling of the Hverfjall eruptive deposits; (a) Location of the Krafla Volcanic System (KVS) in the larger tectonic setting of Iceland; (b) Hverfjall tuff ring viewed from the north; (c) Detailed map of the study area, with annotated locations of sampling sites from Table 1. Redrawn from Liu et al., (2017); (d) Stratigraphic section at site H<sub>6.3</sub> where hydromagmatic and magmatic deposits are exposed together, also showing underlying Hekla-3 silicic ash deposit. Tape measure is 70 cm for scale; (e) Characteristic erosion patterns in hydromagmatic base surge deposits at site H<sub>8.9</sub>, viewed from the north.

**Figure 2:** Textural properties of erupted pyroclasts; (a) Hydromagmatic fall deposit [3φ; H<sub>6.3</sub>]; (b) Plagioclase-Clinopyroxene-Olivine glomerocryst with associated Fe-Cu-Ni sulfide globules [H<sub>2.3</sub>]. Olivine has been outlined in red for clarity; (c) Skeletal olivine morphology [H<sub>2.3</sub>]; (d) Recycled crystalline lithic (cognate and/or accessory) within juvenile sideromelane clast [H<sub>2.3</sub>].

**Figure 3:** Major element matrix glass composition expressed as weight percent anhydrous oxides, for the Hverfjall Fires hydromagmatic fall (blue), hydromagmatic surge (green) and magmatic fall (red) deposits. Melt inclusion compositions are represented by orange (olivine-hosted) and black (plagioclase-hosted) crosses; (a) SiO<sub>2</sub> vs. K<sub>2</sub>O; (b) MgO vs. FeO<sub>T</sub>; (c) MgO vs. Al<sub>2</sub>O<sub>3</sub>; (d) MgO vs. CaO. Data for Hverfjall are presented in Table S1, supplementary information. Solid lines show reverse fractional crystallisation liquid lines of descent (LLD) starting from the average hydromagmatic matrix glass compositions, modelled using Petrolog3 (Danyushevsky and Plechov, 2011); see main text for details. Whole rock (WR) data for Krafla caldera lavas from Nicholson et al., (1991).

**Figure 4:** Compilation of dissolved sulfur concentrations in matrix glass (coloured symbols) and melt inclusions (black crosses). Matrix glasses analyses are coloured according to deposit type (hydromagmatic fall [blue] hydromagmatic surge [green], magmatic scoria [red]) and clast morphology (dense fragment [diamond], shard [triangle], or vesicular particle [circle]). All clasts analysed are >0φ (<1 mm), with the exception of 20 clasts in the sample H<sub>2.3</sub> (2–4 mm) and two lapilli in M<sub>Q1</sub> (16–32 mm). Data presented in Table S1, supplementary information.



**Figure 5:** Co-variation in dissolved sulfur and chlorine concentrations in hydromagmatic fall (blue filled symbols) and magmatic (red open symbols) matrix glasses, and melt inclusions (black crosses) from Figure 5. Data presented in Table S1, supplementary information.

**Figure 6:** Core-to-rim profiles of matrix glass sulfur concentrations in 16–32 mm lapilli clasts [M<sub>Q1</sub>], showing the transition from quenched rim to expanded core. Symbols are coloured according to their position within the sample: rim (filled circles) or core (crosses). The backscattered electron SEM image illustrates the locations of analysis points for ‘clast 1’ for comparison with corresponding changes in vesicle texture. Analysis points are annotated with their sulfur concentration in ppm.

**Figure 7:** Co-variation in sulfur (ppm; measured by electron microprobe) and H<sub>2</sub>O (wt%; measured by FTIR spectroscopy) concentrations in matrix glasses from magmatic (red triangles; H<sub>Q1</sub>) and hydromagmatic (blue circles; H<sub>2.3</sub>) pyroclasts from the 0φ (1–2 mm) size class (Table S2, supplementary information). Open symbols indicate those glasses that contained measurable CO<sub>2</sub> above the detection limit of 4 ppm. The filled square shows the H<sub>2</sub>O concentration in equilibrium with 1 atm pressure for Kīlauean ocean island basalts (0.09 ± 0.003 wt%; Wallace and Anderson, 1998; Mangan et al., 1993; Cashman et al., 1994; Mastin et al., 2004).

**Figure 8:** Thermodynamic modelling of C-O-H-S as a function of pressure using SolEx (Witham et al., 2012). Model runs were initiated using full parameterisation of the average hydromagmatic glass composition (Table S1), and initial volatile concentrations of 1.2 wt% CO<sub>2</sub>, 0.6 wt% H<sub>2</sub>O, 1500 ppm S, and 160 ppm Cl. Temperature and oxygen fugacity were fixed at 1150 °C and NNO=0.5, respectively.

698

699 **Figure 9:** Volatile saturation pressures of hydromagmatic glasses (from Figure 8) translated to  
700 physical depths, for either lithostatic (open symbols) or hydrostatic (filled symbols) pressure  
701 gradients. The different symbols explore the effect of variable assumed CO<sub>2</sub> contents (0, 5, and  
702 20 ppm) below the FTIR detection limit on the calculated pressures/depths.

703

704 **Figure 10:** Sulfur degassing in Ocean Island Basalts; (a) Compilation of sulfur concentrations  
705 for matrix glass (coloured symbols) and melt inclusions (black open symbols) from Icelandic  
706 glasses as a function of TiO<sub>2</sub>/FeO (wt%), for a range of different Icelandic basaltic systems,  
707 including Hverfjall (circles; Table S1, this study), Veidivötn (vertical crosses; Þórðarson et al.,  
708 2003), Holuhraun (6-point stars; Gauthier et al., 2016), Laki (diamonds; Þórðarson et al., 1996),  
709 Grímsvötn (horizontal crosses; Sigmarsson et al., 2013; Liu et al., 2015), Katla (squares;  
710 Þórðarson et al., 2003; Óladóttir et al., 2008), Fimmsvörðuhals (5-point stars; Þórðarson et al.,  
711 2011), and Surtsey (triangles; Schipper et al., 2015). The range of sulfur concentrations within  
712 the deposits of Icelandic tuyas are shown by the vertical arrows, for subaerial lava flows (red  
713 arrow) and subaqueous deposits >400 m water depth (blue arrow; Moore and Calk, 1991). (b)  
714 Sulfur concentration of matrix glass and melt inclusions as a function of FeO wt% for Icelandic  
715 (large symbols) and Hawaiian (small symbols; Kīlauea) glasses, for comparison. Data for  
716 Kīlauea from Mastin et al., (2004), Sides et al., (2014), and Moussallam et al., (2016). The  
717 colour scheme for symbols is the same as (a). The black line corresponds to the theoretical  
718 sulfur content at sulfide saturation (SCSS) for Fe-S-O-liquid-saturated MORB melts,  
719 illustrating the dependence of sulfur solubility on melt FeO composition (Wallace and  
720 Carmichael, 1992; Mavrogenes and O'Neill, 1999, Wallace and Edmonds, 2011).

721

**Figure 11:** Vesicularity as a function of pressure for mafic melts at 1125 °C, for different initial H<sub>2</sub>O contents (from Pioli et al., 2008), showing the range of vesicularities in hydromagmatic pyroclasts from Hverfjall (light blue shaded region; Liu et al., 2017) and the range of saturation pressures calculated in this study from glass volatile concentrations in the same deposits (grey shaded region). Symbols represent independent empirical measurements of vesicularity as a function of pressure for other volcanic systems in Iceland where quench pressure is well-constrained. <sup>1</sup>Dredge samples of pillow basalt rims from varying water depths off the Reykjanes Peninsula (grey crosses; Moore and Schilling, 1973); <sup>2</sup>Subglacial pillow basalt rims within Icelandic tuyas emplaced beneath ice of known thicknesses (black triangles; Jones, 1969).

## Tables

**Table 1:** Details of the main samples used in this study. <sup>a</sup> Distance from centre of Jarðbaðshólar vent if ‘dry’ magmatic or Hverfjall vent if hydromagmatic.

Sample name		Origin	Deposit Type	GPS Location (minutes/ degrees/ seconds)	Distance from the vent <sup>a</sup> (km)
H <sub>2,3</sub>		Hydromagmatic	Fall	65 35 39.6 N 16 51 38.3 W	1.5
H <sub>6,3</sub>		Hydromagmatic	Fall	65 37 57.4 N 16 50 38.0 W	3.5
H <sub>9,3</sub>		Hydromagmatic	Fall	65 38 36.1 N 16 52 17.6 W	4.5
H <sub>7,5</sub>		Hydromagmatic	Fall	65 39 25.6 N 16 34 02.0 W	15
H <sub>crater</sub>	E (top)	Hydromagmatic	Fall/Surge	65 36 30.3 N 16 52 44.9 W	0
	C				
	A (base)				
H <sub>8,9</sub>	F (top)	Hydromagmatic	Surge	65 37 00.9 N 16 51 27.6 W	1.5
	E				
	D				
	C				
	B				
	A (base)				
M <sub>Q1</sub>		Magmatic (dry)	Fall	65 37 55.2 N 16 50 59.4 W	0.4
M <sub>6,3</sub>		Magmatic (dry)	Fall	65 37 57.4 N 16 50 38.0 W	0.5
M <sub>Q3</sub>		Magmatic (dry)	Fall	65 38 13.8 N 16 51 11.8 W	0.2

## References

- Agustín-Flores, J., Németh, K., Cronin, S. J., Lindsay, J. M., Kereszturi, G., Brand, B. D. & Smith, I. E. (2014), Phreatomagmatic eruptions through unconsolidated coastal plain sequences, Maungataketake, Auckland volcanic field (New Zealand), *Journal of Volcanology and Geothermal Research* 276, 46–63.
- Büttner, R., Dellino, P., La Volpe, L., Lorenz, V. & Zimanowski, B. (2002), Thermohydraulic explosions in phreatomagmatic eruptions as evidenced by the comparison between pyroclasts and products from Molten Fuel Coolant Interaction experiments, *Journal of Geophysical Research - Solid Earth* 107(B11), 2277.
- Carroll, M. & Rutherford, M. J. (1988), Sulfur speciation in hydrous experimental glasses of varying oxidation state – results from measured wave-length shifts of sulfur X-rays, *American Mineralogist* 73(7), 845–9.
- Cashman, K. & Scheu, B. (2015), Magma Fragmentation, in Sigurdsson, Haraldur and Houghton, Bruce and McNutt, Steve and Rymer, Hazel and Stix, John, ed., ‘Encyclopedia of Volcanoes’, Elsevier, pp. 459–475.
- Cashman, K. V., Mangan, M. T. & Newman, S. (1994), Surface degassing and modifications to vesicle size distributions in active basalt flows, *Journal of Volcanology and Geothermal Research* 61(1-2), 45–68.
- Cole, P., Guest, J., Duncan, A. & Pacheco, J.-M. (2001), Capelinhos 1957– 1958, Faial, Azores: deposits formed by an emergent Surtseyan eruption, *Bulletin of volcanology* 63(2-3), 204–220.
- Colgate, S. A. & Sigurgeirsson, T. (1973), Dynamic mixing of water and lava, *Nature* 244, 552–555.

775 Danyushevsky, L. V. (2001), The effect of small amounts of H<sub>2</sub>O on crystallisation of mid-  
776 ocean ridge and backarc basin magmas, *Journal of Volcanology and Geothermal Research*  
777 110(3-4), 265–280.

778 Danyushevsky, L.V. and Plechov, P., (2011), Petrolog3: Integrated software for modeling  
779 crystallization processes, *Geochemistry, Geophysics, Geosystems*, 12(7).

780 Davis, M.G., Garcia, M.O. and Wallace, P., 2003. Volatiles in glasses from Mauna Loa  
781 Volcano, Hawai'i: implications for magma degassing and contamination, and growth of  
782 Hawaiian volcanoes. *Contributions to Mineralogy and Petrology*, 144(5), 570-591.

783 Dingwell, D. B. & Webb, S. L. (1989), Structural relaxation in silicate melts and non-  
784 Newtonian melt rheology in geologic processes, *Physics and Chemistry of Minerals*, 16(5),  
785 508–516.

786 Dixon, J. E. (1997), Degassing of alkalic basalts, *American Mineralogist*, 82(3-4), 368–378.

787 Dixon, J. E., Clague, D. A. & Stolper, E. M. (1991), Degassing history of water, sulfur, and  
788 carbon in submarine lavas from Kīlauea Volcano, Hawai'i, *The Journal of Geology*, 99(3),  
789 371–394.

790 Dixon, J. E., Stolper, E. & Delaney, J. R. (1988), Infrared spectroscopic measurements of CO<sub>2</sub>  
791 and H<sub>2</sub>O in Juan de Fuca Ridge basaltic glasses, *Earth and Planetary Science Letters* 90(1),  
792 87–104.

793 Dixon, J. E., Stolper, E. M. & Holloway, J. R. (1995), An experimental study of water and  
794 carbon dioxide solubilities in mid-ocean ridge basaltic liquids. Part I: calibration and solubility  
795 models, *Journal of Petrology* 36(6), 1607–1631.

796 Dixon, J.E., Filiberto, J.R., Moore, J.G. and Hickson, C.J., 2002. Volatiles in basaltic glasses  
797 from a subglacial volcano in northern British Columbia (Canada): implications for ice sheet

798 thickness and mantle volatiles. Geological Society, London, Special Publications, 202(1), 255-  
799 271.

800 Edmonds, M. (2008), New geochemical insights into volcanic degassing, Philosophical  
801 Transactions of the Royal Society of London A: Mathematical, Physical and Engineering  
802 Sciences 366(1885), 4559–4579.

803 Edmonds, M. & Mather, T. A. (2017), Volcanic sulfides and outgassing, Elements 13(2), 105–  
804 110.

805 Edmonds, M. & Wallace, P. J. (2017), Volatiles and Exsolved Vapor in Volcanic Systems,  
806 Elements 13(1), 29–34.

807 Edwards, B.R., Skilling, I.P., Cameron, B., Haynes, C., Lloyd, A. and Hungerford, J.H., 2009.  
808 Evolution of an englacial volcanic ridge: Pillow Ridge tindar, Mount Edziza volcanic complex,  
809 NCVP, British Columbia, Canada. Journal of Volcanology and Geothermal Research, 185(4),  
810 251-275.

811 Einarsson, A. (1982), The palaeolimnology of Lake Mývatn, northern Iceland: plant and  
812 animal microfossils in the sediment, Freshwater Biology 12(1), 63–82.

813 Fine, G. & Stolper, E. (1986), Dissolved carbon dioxide in basaltic glasses: concentrations and  
814 speciation, Earth and Planetary Science Letters 76(3), 263–278.

815 Freda, C., Baker, D. R. & Scarlato, P. (2005), Sulfur diffusion in basaltic melts, Geochimica et  
816 Cosmochimica Acta 69(21), 5061–5069.

817 Gauthier, P.J., Sigmarsson, O., Gouhier, M., Haddadi, B. & Moune, S. (2016), Elevated gas  
818 flux and trace metal degassing from the 2014-2015 fissure eruption at the Barðarbunga volcanic  
819 system, Iceland, Journal of Geophysical Research: Solid Earth.

820 Gerlach, T. M. (1986), Exsolution of H<sub>2</sub>O, CO<sub>2</sub>, and S during eruptive episodes at Kīlauea  
821 Volcano, Hawai'i, *Journal of Geophysical Research: Solid Earth* 91(B12), 12177–12185.

822 Graettinger, A.H. and Valentine, G.A., 2017. Evidence for the relative depths and energies of  
823 phreatomagmatic explosions recorded in tephra rings. *Bulletin of Volcanology*, 79(12), p.88.

824 Grættinger, A., Valentine, G., Sonder, I., Ross, P.S. & White, J. (2015), Facies distribution of  
825 ejecta in analog tephra rings from experiments with single and multiple subsurface explosions,  
826 *Bulletin of Volcanology* 77(8), 1– 12.

827 Grættinger, A., Valentine, G., Sonder, I., Ross, P.-S., White, J. & Taddeucci, J. (2014), Maar-  
828 diatreme geometry and deposits: Subsurface blast experiments with variable explosion depth,  
829 *Geochemistry, Geophysics, Geosystems* 15(3), 740–764.

830 Graettinger, A.H., Skilling, I., McGarvie, D. and Höskuldsson, Á., 2013. Subaqueous basaltic  
831 magmatic explosions trigger phreatomagmatism: a case study from Askja, Iceland. *Journal of*  
832 *Volcanology and Geothermal Research*, 264, pp.17-35.

833 Hartley, M. E., MacLennan, J., Edmonds, M. & Þórðarson, T. (2014), Reconstructing the deep  
834 CO<sub>2</sub> degassing behaviour of large basaltic fissure eruptions, *Earth and Planetary Science*  
835 *Letters* 393, 120–131.

836 Helo, C., Clague, D.A., Dingwell, D.B. and Stix, J., 2013. High and highly variable cooling  
837 rates during pyroclastic eruptions on Axial Seamount, Juan de Fuca Ridge. *Journal of*  
838 *Volcanology and Geothermal Research*, 253, pp.54-64.

839 Helz, R., Cottrell, E., Brounce, M. N. & Kelley, K. A. (2017), Olivine- melt relationships and  
840 syn-eruptive redox variations in the 1959 eruption of Kīlauea Volcano as revealed by XANES,  
841 *Journal of Volcanology and Geothermal Research* 333, 1–14.



842 Houghton, B., White, J. & Van Eaton, A. (2015), Phreatomagmatic and Related Eruption  
843 Styles, in Sigurdsson, Haraldur and Houghton, Bruce and McNutt, Steve and Rymer, Hazel  
844 and Stix, John, ed., 'Encyclopedia of Volcanoes', Elsevier, 537–552.

845 Hungerford, J.D., Edwards, B.R., Skilling, I.P. and Cameron, B.I., 2014. Evolution of a  
846 subglacial basaltic lava flow field: Tennena volcanic center, Mount Edziza volcanic complex,  
847 British Columbia, Canada. *Journal of Volcanology and Geothermal Research*, 272, 39-58.

848 Johnson, E. R., Wallace, P. J., Cashman, K. V. & Granados, H. D. (2010), Degassing of  
849 volatiles (H<sub>2</sub>O, CO<sub>2</sub>, S, Cl) during ascent, crystallization, and eruption at mafic monogenetic  
850 volcanoes in central Mexico, *Journal of Volcanology and Geothermal Research* 197(1-4), 225–  
851 238.

852 Jones, J. (1969), Pillow lavas as depth indicators, *American Journal of Science* 267(2), 181–  
853 195.

854 Jugo, P. J., Wilke, M. & Botcharnikov, R. E. (2010), Sulfur K-edge XANES analysis of natural  
855 and synthetic basaltic glasses: Implications for S speciation and S content as function of  
856 oxygen fugacity, *Geochimica et Cosmochimica Acta* 74(20), 5926–5938.

857 Kokelaar, B. (1983), The mechanism of Surtseyan volcanism, *Journal of the Geological*  
858 *Society* 140(6), 939–944.

859 Kokelaar, P. (1986), Magma-water interactions in subaqueous and emergent basaltic, *Bulletin*  
860 *of Volcanology* 48(5), 275–289.

861 Lefebvre, N.S., White, J.D.L. and Kjarsgaard, B.A., (2012). Spatter-dike reveals subterranean  
862 magma diversions: Consequences for small multivert basaltic eruptions. *Geology*, 40(5), 423-  
863 426.

864 Lefebvre, N.S., White, J.D. and Kjarsgaard, B.A., (2016). Arrested diatreme development:  
 865 Standing Rocks East, Hopi Buttes, Navajo Nation, USA. *Journal of Volcanology and*  
 866 *Geothermal Research*, 310, 186-208.

867 Lesne, P., Kohn, S. C., Blundy, J., Witham, F., Botcharnikov, R. E. & Behrens, H. (2011),  
 868 Experimental simulation of closed-system degassing in the system basalt–H<sub>2</sub>O–CO<sub>2</sub>–S–Cl,  
 869 *Journal of Petrology* 52 (9), 1737-1762.

870 Liu, E.J., Cashman, K., Rust, A. & Höskuldsson, A. (2017), Contrasting mechanisms of magma  
 871 fragmentation during coeval magmatic and hydromagmatic activity: the Hverfjall Fires fissure  
 872 eruption, Iceland, *Bulletin of Volcanology* 79(10), 68.

873 Liu, E., Cashman, K., Rust, A. & Gislason, S. (2015), The role of bubbles in generating fine  
 874 ash during hydromagmatic eruptions, *Geology* 43(3), 239– 242.

875 Liu, Y., Samaha, N.-T. & Baker, D. R. (2007), Sulfur concentration at sulfide saturation  
 876 (SCSS) in magmatic silicate melts, *Geochimica et Cosmochimica Acta* 71(7), 1783–1799.

877 Lloyd, A. S., Plank, T., Ruprecht, P., Hauri, E. H. & Rose, W. (2013), Volatile loss from melt  
 878 inclusions in pyroclasts of differing sizes, *Contributions to Mineralogy and Petrology* 165(1),  
 879 129–153.

880 Lorenz, V. (1975), Formation of phreatomagmatic maar-diatreme volcanoes and its relevance  
 881 to kimberlite diatremes, *Physics and Chemistry of the Earth* 9, 17–27.

882 Lorenz, V. (1986), On the growth of maars and diatremes and its relevance to the formation of  
 883 tuff rings, *Bulletin of Volcanology* 48(5), 265–274.

884 Lorenz, V. (2003), Maar-diatreme volcanoes, their formation, and their setting in hard-rock or  
 885 soft-rock environments, *Geolines* 15, 72–83.

886 Mangan, M. & Cashman, K. (1996), The structure of basaltic scoria and reticulite and  
887 inferences for vesiculation, foam formation, and fragmentation in lava fountains, *Journal of*  
888 *Volcanology and Geothermal Research* 73(1-2), 1–18.

889 Mangan, M., Cashman, K. & Newman, S. (1993), Vesiculation of basaltic magma during  
890 eruption, *Geology* 21(2), 157–160.

891 Mangan, M. T., Cashman, K. V. & Swanson, D. A. (2014), The dynamics of Hawaiian-style  
892 eruptions: a century of study, in Poland, MP and Takahashi, TJ and Landowski, CM, ed.,  
893 ‘Characteristics of Hawaiian volcanoes’, US Geological Survey, 323–354.

894 Mastin, L. G. (1997), Evidence for water influx from a caldera lake during the explosive  
895 hydromagmatic eruption of 1790, Kīlauea volcano, Hawaii, *Journal of Geophysical Research:*  
896 *Solid Earth* 102(B9), 20093–20109.

897 Mastin, L.G., Christiansen, R. L., Thornber, C., Lowenstern, J. & Beeson, M. (2004), What  
898 makes hydromagmatic eruptions violent? Some insights from the Keanakako’i Ash, Kīlauea  
899 Volcano, Hawai’i, *Journal of Volcanology and Geothermal Research* 137(1), 15–31.

900 Mathez, E. (1976), Sulfur solubility and magmatic sulfides in submarine basalt glass, *Journal*  
901 *of Geophysical Research* 81(23), 4269–4276.

902 Mattsson, H. B. (2010), Textural variation in juvenile pyroclasts from an emergent, Surtseyan-  
903 type, volcanic eruption: The Capelas tuff cone, Sao Miguel (Azores), *Journal of Volcanology*  
904 *and Geothermal Research* 189(1), 81–91.

905 Mattsson, H. B. & Höskuldsson, A. (2011), Contemporaneous phreatomagmatic and effusive  
906 activity along the Hverfjall eruptive fissure, north Iceland: Eruption chronology and resulting  
907 deposits, *Journal of Volcanology and Geothermal Research* 201(1), 241–252.

908 Mavrogenes, J. A. & O'Neill, H. S. C. (1999), The relative effects of pressure, temperature and  
 909 oxygen fugacity on the solubility of sulfide in mafic magmas, *Geochimica et Cosmochimica*  
 910 *Acta* 63(7), 1173–1180.

911 Métrich, N. & Wallace, P. J. (2008), Volatile abundances in basaltic magmas and their  
 912 degassing paths tracked by melt inclusions, *Reviews in mineralogy and geochemistry* 69(1),  
 913 363–402.

914 Métrich, N., Bertagnini, A., Di Muro, A. et al. (2010), Conditions of Magma Storage,  
 915 Degassing and Ascent at Stromboli: New Insights into the Volcano Plumbing System with  
 916 Inferences on the Eruptive Dynamics, *Journal of Petrology*.

917 Métrich, N., Sigurdsson, H., Meyer, P. S. & Devine, J. D. (1991), The 1783 Lakagigar eruption  
 918 in Iceland: geochemistry, CO<sub>2</sub> and sulfur degassing, *Contributions to Mineralogy and*  
 919 *Petrology* 107(4), 435–447.

920 Moore, J. G. (1965), Petrology of deep sea basalt near Hawai'i, *American Journal of Science*  
 921 263(1), 40–52.

922 Moore, J. G. & Calk, L. C. (1991), Degassing and differentiation in sub- glacial volcanoes,  
 923 Iceland, *Journal of Volcanology and Geothermal Research* 46(1-2), 157–180.

924 Moore, J. G. & Fabbi, B. P. (1971), An estimate of the juvenile sulfur content of basalt,  
 925 *Contributions to Mineralogy and Petrology* 33(2), 118–127.

926 Moretti, R. & Baker, D. R. (2008), Modeling the interplay of fO<sub>2</sub> and fS<sub>2</sub> along the FeS-silicate  
 927 melt equilibrium, *Chemical Geology* 256(3), 286– 298.

928 Moretti, R., Papale, P. & Ottonello, G. (2003), A model for the saturation of COHS fluids  
 929 in silicate melts, *Geological Society, London, Special Publications* 213(1), 81–101.

930 Neave, D. A., MacLennan, J., Edmonds, M. & Þórðarson, T. (2014), Melt mixing causes  
 931 negative correlation of trace element enrichment and CO<sub>2</sub> content prior to an Icelandic  
 932 eruption, *Earth and Planetary Science Letters* 400, 272–283.

933 Newman, S. & Lowenstern, J. B. (2002), VolatileCalc: a silicate melt–H<sub>2</sub>O–CO<sub>2</sub> solution  
 934 model written in Visual Basic for Excel, *Computers & Geosciences* 28(5), 597–604.

935 Óladóttir, B. A., Sigmarsson, O., Larsen, G. & Þórðarson, T. (2008), Katla volcano, Iceland:  
 936 magma composition, dynamics and eruption frequency as recorded by Holocene tephra layers,  
 937 *Bulletin of Volcanology* 70(4), 475–493.

938 O'Neill, H. S. C. & Mavrogenes, J. A. (2002), The sulfide capacity and the sulfur content at  
 939 sulfide saturation of silicate melts at 1400 C and 1 bar, *Journal of Petrology* 43(6), 1049–1087.

940 Parfitt, E. A. (1998), A study of clast size distribution, ash deposition and fragmentation in a  
 941 Hawaiian-style volcanic eruption, *Journal of Volcanology and Geothermal Research* 84(3),  
 942 197–208.

943 Patten, C., Barnes, S.-J., Mathez, E. A. & Jenner, F. E. (2013), Partition coefficients of  
 944 chalcophile elements between sulfide and silicate melts and the early crystallization history of  
 945 sulfide liquid: LA-ICP-MS analysis of MORB sulfide droplets, *Chemical Geology* 358, 170–  
 946 188.

947 Peckover, R., Buchanan, D. & Ashby, D. (1973), Fuel–coolant interactions in submarine  
 948 vulcanism, *Nature* 245, 307–308.

949 Pioli, L., Erlund, E., Johnson, E., Cashman, K., Wallace, P., Rosi, M. & Granados, H. D.  
 950 (2008), Explosive dynamics of violent Strombolian eruptions: The eruption of Parícutin  
 951 Volcano 1943–1952 (Mexico), *Earth and Planetary Science Letters* 271(1), 359–368.

952 Porritt, L.A., Russell, J. K. & Quane, S.L. (2012), Pele's tears and spheres: Examples from  
 953 Kīlauea Iki, Earth and Planetary Science Letters 333, 171–180.

954 Rausch, J., Grobéty, B. & Vonlanthen, P. (2015), Eifel maars: Quantitative shape  
 955 characterization of juvenile ash particles (Eifel Volcanic Field, Germany), Journal of  
 956 Volcanology and Geothermal Research 291, 86–100.

957 Sæmundsson, K. (1991), Jarðfræði Kroflukerfisins, in Gardarsson, A. and Einarsson, A., ed.,  
 958 'Náttúra Mývatns', 662, Hid íslenska Náttúrufræðifélag, Reykjavík, 24–95.

959 Schipper, C. I. & White, J. D. (2016), Magma-slurry interaction in Surtseyan eruptions,  
 960 Geology, G37480–1.

961 Schipper, C. I., Jakobsson, S. P., White, J. D., Palin, J.M. & Bush-Marcinowski, T. (2015), The  
 962 Surtsey Magma Series, Scientific reports 5, 11498.

963 Schipper, C. I., White, J. D. & Houghton, B. F. (2010), Syn-and post- fragmentation textures  
 964 in submarine pyroclasts from Loihi Seamount, Hawai'i, Journal of Volcanology and  
 965 Geothermal Research 191(1), 93–106.

966 Schipper CI, White JDL, Houghton BF (2011) Textural, geochemical, and volatile evidence  
 967 for a Strombolian-like eruption sequence at Loihi Seamount, Hawaii. J Volcanol Geotherm Res  
 968 207:16-32. doi:10.1016/j.jvolgeores.2011.08.001

969 Schipper CI, White JDL, Houghton BF, Shimizu N, Stewart RB (2010a) Explosive submarine  
 970 eruptions driven by volatile-coupled degassing at Lō`ihi Seamount, Hawai`i. Earth Planet Sci  
 971 Lett 295:497-510. doi:10.1016/j.epsl.2010.04.031

972 Schipper CI, White JDL, Houghton BF, Shimizu N, Stewart RB (2010b) "Poseidic" explosive  
 973 eruptions at Loihi Seamount, Hawaii. Geology 38:291-294. doi:doi: 10.1130/G30351.1

974 Self, S., Blake, S., Sharma, K., Widdowson, M. & Sephton, S. (2008), Sulfur and chlorine in  
 975 Late Cretaceous Deccan magmas and eruptive gas release, *Science* 319(5870), 1654–1657.

976 Sheridan, M. F. & Wohletz, K. H. (1983), Hydrovolcanism: basic considerations and review,  
 977 *Journal of Volcanology and Geothermal Research* 17(1), 1–29.

978 Sides, I., Edmonds, M., MacLennan, J., Swanson, D. & Houghton, B. (2014), Eruption style at  
 979 Kīlauea Volcano in Hawai‘i linked to primary melt composition, *Nature Geoscience* 7(6), 464.

980 Sigmarsson, O., Haddadi, B., Carn, S., Moune, S., Gudnason, J., Yang, K. & Clarisse, L.  
 981 (2013), The sulfur budget of the 2011 Grimsvötn eruption, Iceland, *Geophysical Research*  
 982 *Letters* 40(23), 6095–6100.

983 Stolper, E. (1982), Water in silicate glasses: an infrared spectroscopic study, *Contributions to*  
 984 *Mineralogy and Petrology* 81(1), 1–17.

985 Swanson, D.A. & Fabbi, B. P. (1973), Loss of volatiles during fountaining and flowage of  
 986 basaltic lava at Kīlauea volcano, Hawai‘i, *Journal of Research of the US Geological Survey*  
 987 1(6), 649–658.

988 Þórarinnsson, S. (1967), *Surtsey: The new island in the North Atlantic*, Viking Press.

989 Þórarinnsson, S. (1979), The postglacial history of the Mývatn area, *Oikos*, 17–28.

990 Þórðarson, T. & Self, S. (2003), Atmospheric and environmental effects of the 1783–1784 Laki  
 991 eruption: A review and reassessment, *Journal of Geophysical Research: Atmospheres* 108(D1),  
 992 2156–2202.

993 Þórðarson, T., Hayward, C., Moune, S., Hartley, M., Sigmarsson, O., Höskuldsson, A.,  
 994 Guðmundsson, M. & Sigmundsson, F. (2011), The 20 March–12 April 2010 Fimmvorðuhals  
 995 eruption, Eyjafjallajökull volcano, Iceland: Volatile contents and magma degassing,  
 996 *Geophys. Research Abstracts* 13, EGU2011–12147.

997 Þórðarson, T., Miller, D., Larsen, G., Self, S. & Sigurdsson, H. (2001), New estimates of  
 998 sulfur degassing and atmospheric mass-loading by the 934 AD Eldgja eruption, Iceland,  
 999 *Journal of Volcanology and Geothermal Research* 108(1), 33–54.

1000 Þórðarson, T., Self, S., Miller, D., Larsen, G. & Vilmundardottir, E. (2003), Sulphur release  
 1001 from flood lava eruptions in the Veidivötn, Grimsvötn and Katla volcanic systems, Iceland,  
 1002 *Geological Society, London, Special Publications* 213(1), 103–121.

1003 Þórðarson, T., Self, S., Oskarsson, N. & Hulsebosch, T. (1996), Sulfur, chlorine, and fluorine  
 1004 degassing and atmospheric loading by the 1783–1784 AD Laki (Skaftar Fires) eruption in  
 1005 Iceland, *Bulletin of Volcanology* 58(2-3), 205–225.

1006 Toplis, M. (2005), The thermodynamics of iron and magnesium partitioning between olivine  
 1007 and liquid: criteria for assessing and predicting equilibrium in natural and experimental  
 1008 systems, *Contributions to Mineralogy and Petrology* 149(1), 22–39.

1009 Valentine, G. A., Grättinger, A. H. & Sonder, I. (2014), Explosion depths for phreatomagmatic  
 1010 eruptions, *Geophysical Research Letters*, 41(9), 3045–3051.

1011 Valentine, G. A., Sottili, G., Palladino, D. M. & Taddeucci, J. (2015), Tephra ring interpretation  
 1012 in light of evolving maar–diatreme concepts: Stracciacappa maar (central Italy), *Journal of*  
 1013 *Volcanology and Geothermal Research* 308, 19–29.

1014 Valentine, G. A., White, J. D., Ross, P.-S., Graettinger, A. H. & Sonder, I. (2017), Updates to  
 1015 Concepts on Phreatomagmatic Maar-Diatremes and Their Pyroclastic Deposits, *Frontiers in*  
 1016 *Earth Science* 5, 68.

1017 Van Otterloo, J., Cas, R. A. & Scutter, C. R. (2015), The fracture behaviour of volcanic glass  
 1018 and relevance to quench fragmentation during formation of hyaloclastite and  
 1019 phreatomagmatism, *Earth-Science Reviews* 154, 79–116.



1020 Wagh, A.S., Singh, J.P. and Poeppel, R.B. (1993). Dependence of ceramic fracture properties  
1021 on porosity. *Journal of materials science*, 28(13), 3589–3593.

1022 Wallace, P. & Carmichael, I. S. (1992), Sulfur in basaltic magmas, *Geochimica et*  
1023 *Cosmochimica Acta* 56(5), 1863–1874.

1024 Wallace, P. J. (2003), From mantle to atmosphere: magma degassing, explosive eruptions, and  
1025 volcanic volatile budgets, in ‘*Developments in volcanology*’, 5, Elsevier, 105–127.

1026 Wallace, P. J. & Anderson Jr, A. T. (1998), Effects of eruption and lava drainback on the H<sub>2</sub>O  
1027 contents of basaltic magmas at Kīlauea Volcano, *Bulletin of Volcanology* 59(5), 327–344.

1028 Wallace, P. J. & Edmonds, M. (2011), The sulfur budget in magmas: Evidence from melt  
1029 inclusions, submarine glasses, and volcanic gas emissions, *Reviews in Mineralogy and*  
1030 *Geochemistry* 73(1), 215–246.

1031 Wallace, P. J., Plank, T., Edmonds, M. & Hauri, E. H. (2015), Chapter 7 - Volatiles in Magmas,  
1032 in H. Sigurdsson, ed., ‘*The Encyclopedia of Volcanoes (Second Edition)*’, Academic Press,  
1033 Amsterdam, 163 – 183.

1034 White, J. D. (1996), Impure coolants and interaction dynamics of phreatomagmatic eruptions,  
1035 *Journal of Volcanology and Geothermal Research* 74(3), 155–170.

1036 White, J. D. & Valentine, G. A. (2016), Magmatic versus phreatomagmatic fragmentation:  
1037 Absence of evidence is not evidence of absence, *Geosphere* 12(5), 1478–1488.

1038 Witham, F., Blundy, J., Kohn, S.C., Lesne, P., Dixon, J., Churakov, S.V. & Botcharnikov, R.  
1039 (2012), SolEx: A model for mixed COHSCl-volatile solubilities and exsolved gas compositions  
1040 in basalt, *Computers and Geosciences* 45, 87–97.

1041 Wohletz, K. H. (1986), Explosive magma-water interactions: Thermodynamics, explosion  
1042 mechanisms, and field studies, *Bulletin of Volcanology* 48(5), 245–264.

1043 Wright, H. M., Cashman, K. V., Rosi, M. & Cioni, R. (2007), Breadcrust bombs as indicators  
 1044 of Vulcanian eruption dynamics at Guagua Pichincha volcano, Ecuador, *Bulletin of*  
 1045 *Volcanology* 69(3), 281–300.

1046 Zhang, Y. & Stolper, E. M. (1991), Water diffusion in a basaltic melt, *Nature* 351(6324), 306.

1047 Zimanowski, B., Büttner, R., Lorenz, V. & Hafele, H.-G. (1997), Fragmentation of basaltic  
 1048 melt in the course of explosive volcanism, *Journal of Geophysical Research: Solid Earth*  
 1049 102(B1), 803–814.

1050 Zimanowski, B., Fröhlich, G. & Lorenz, V. (1991), Quantitative experiments on  
 1051 phreatomagmatic explosions, *Journal of Volcanology and Geothermal Research* 48(3), 341–  
 1052 358.

Figure 1

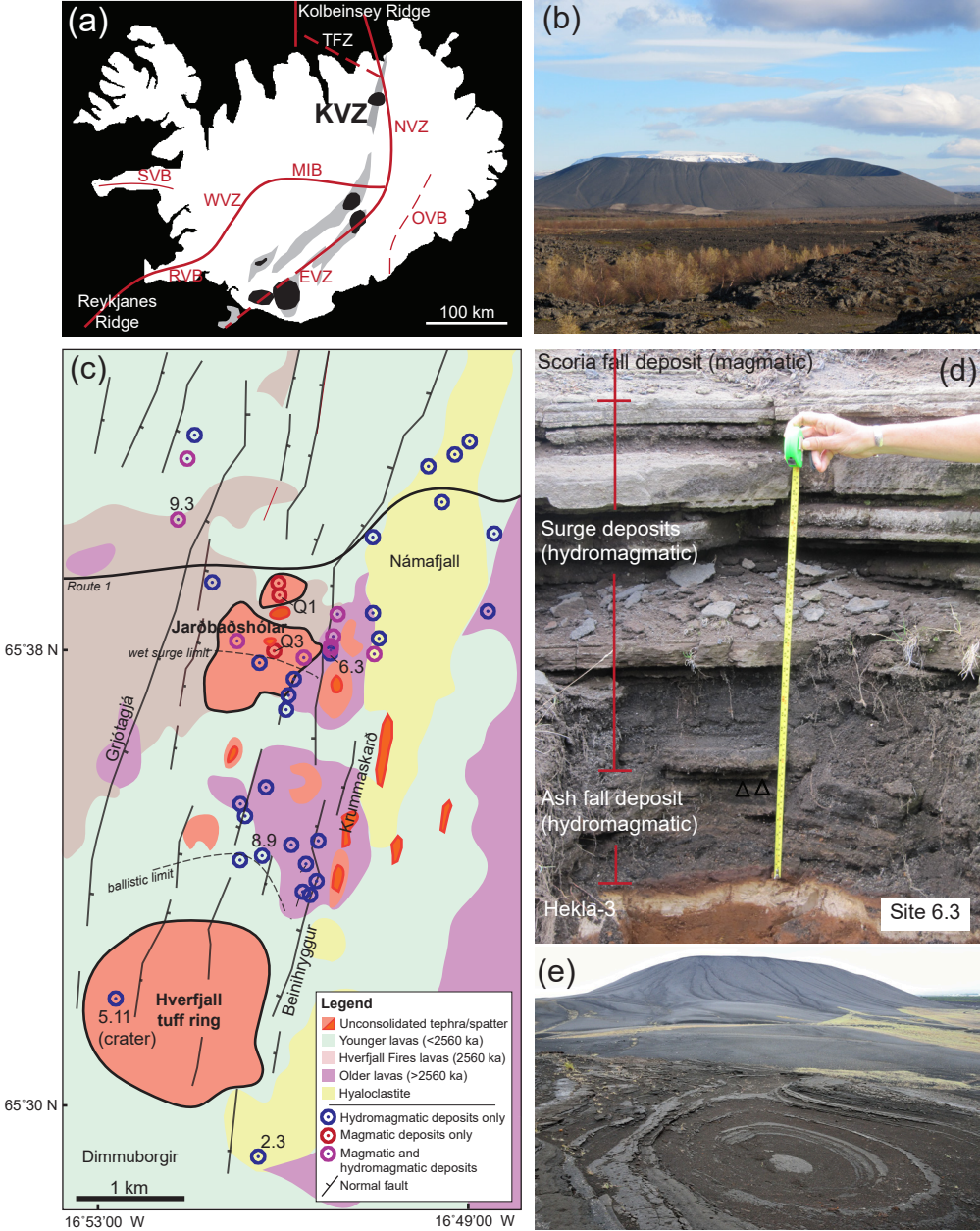


Figure 2

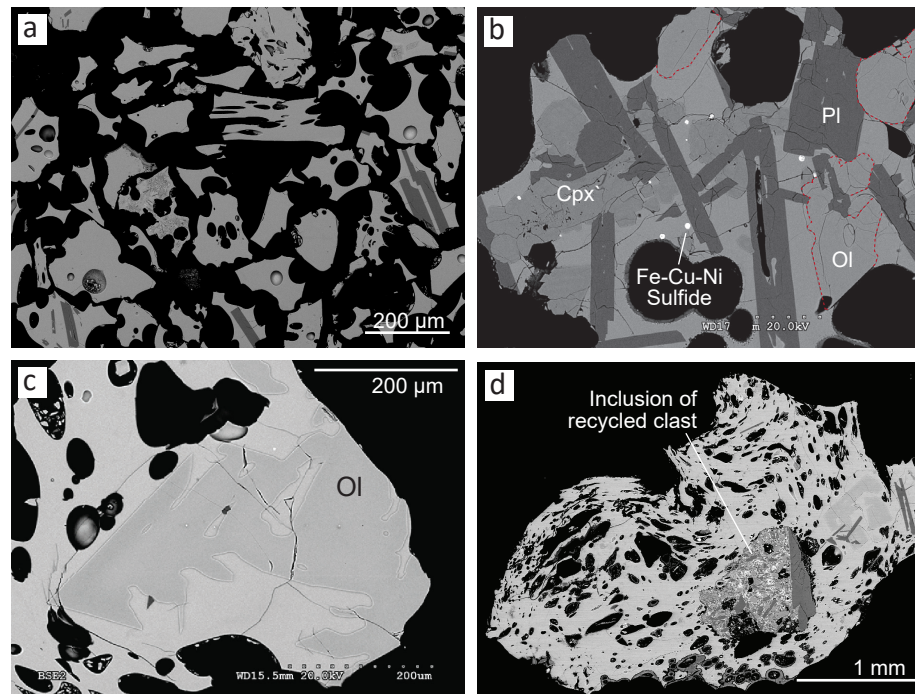


Figure 3

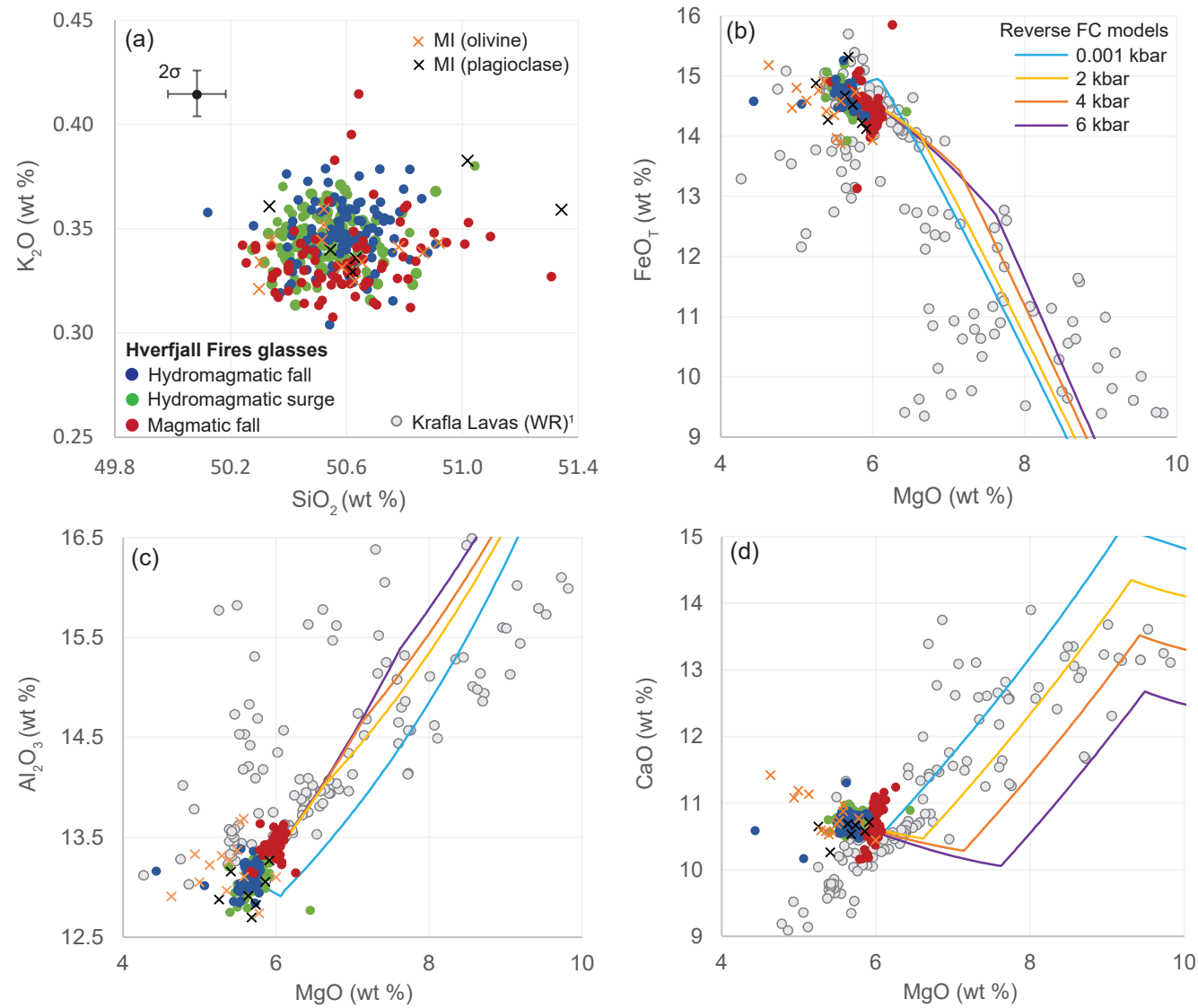


Figure 4

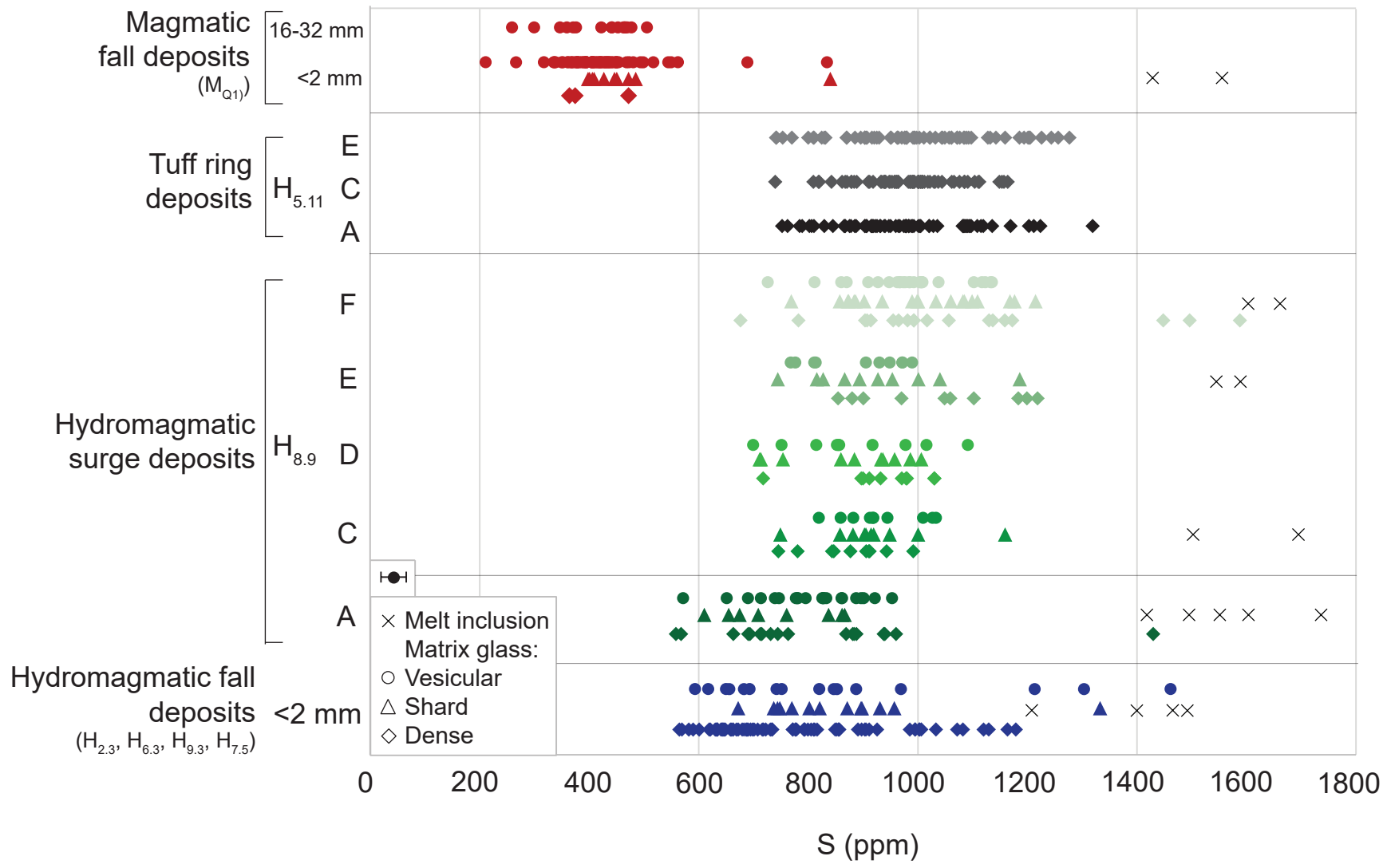


Figure 5

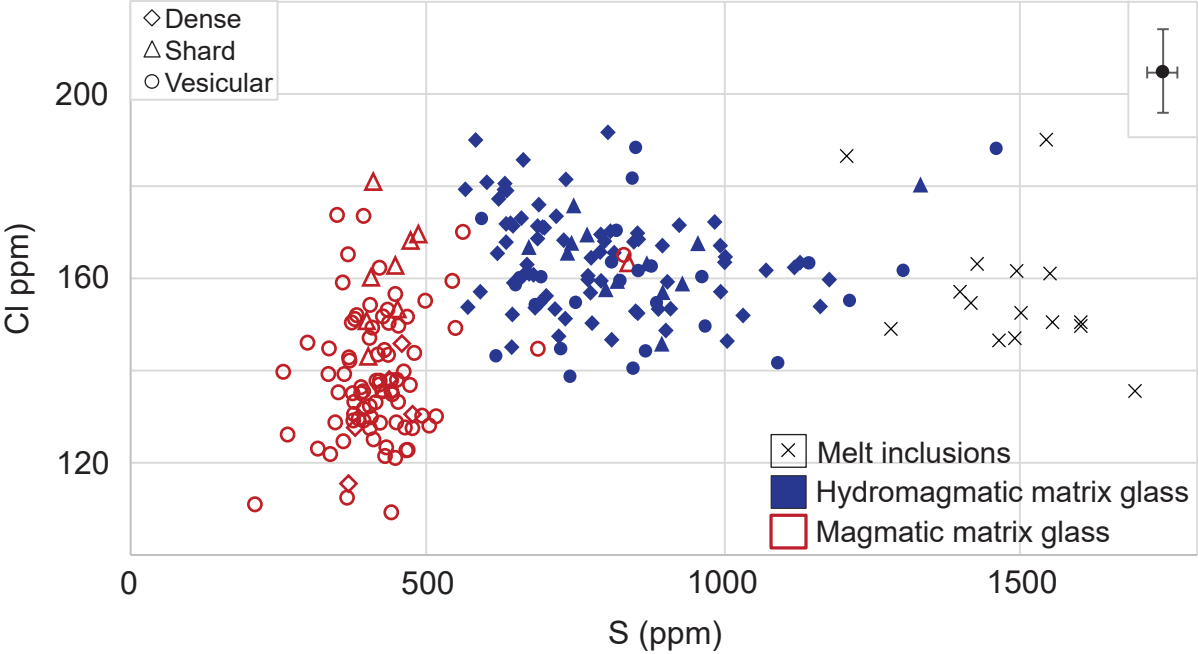


Figure 6

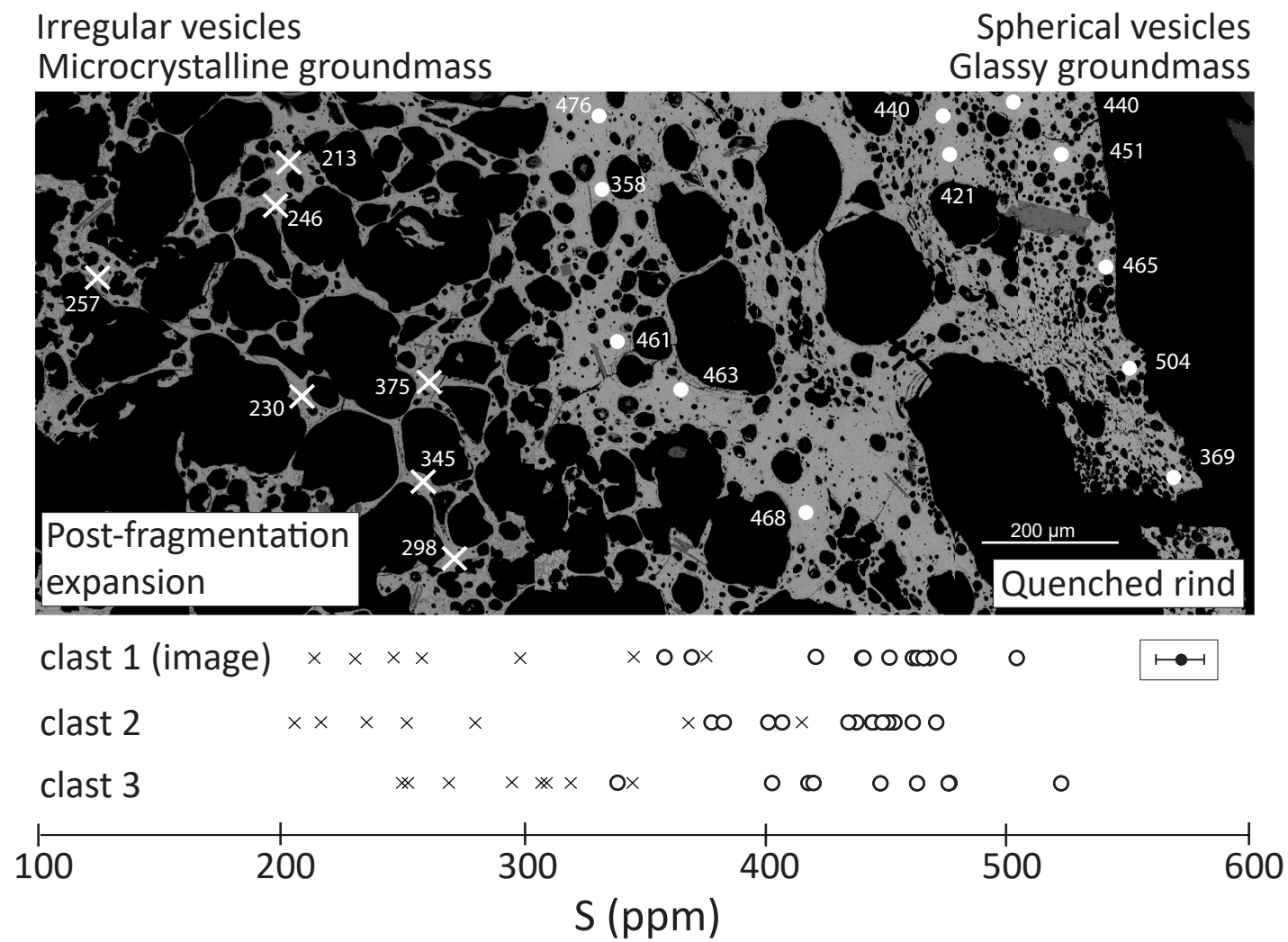




Figure 7

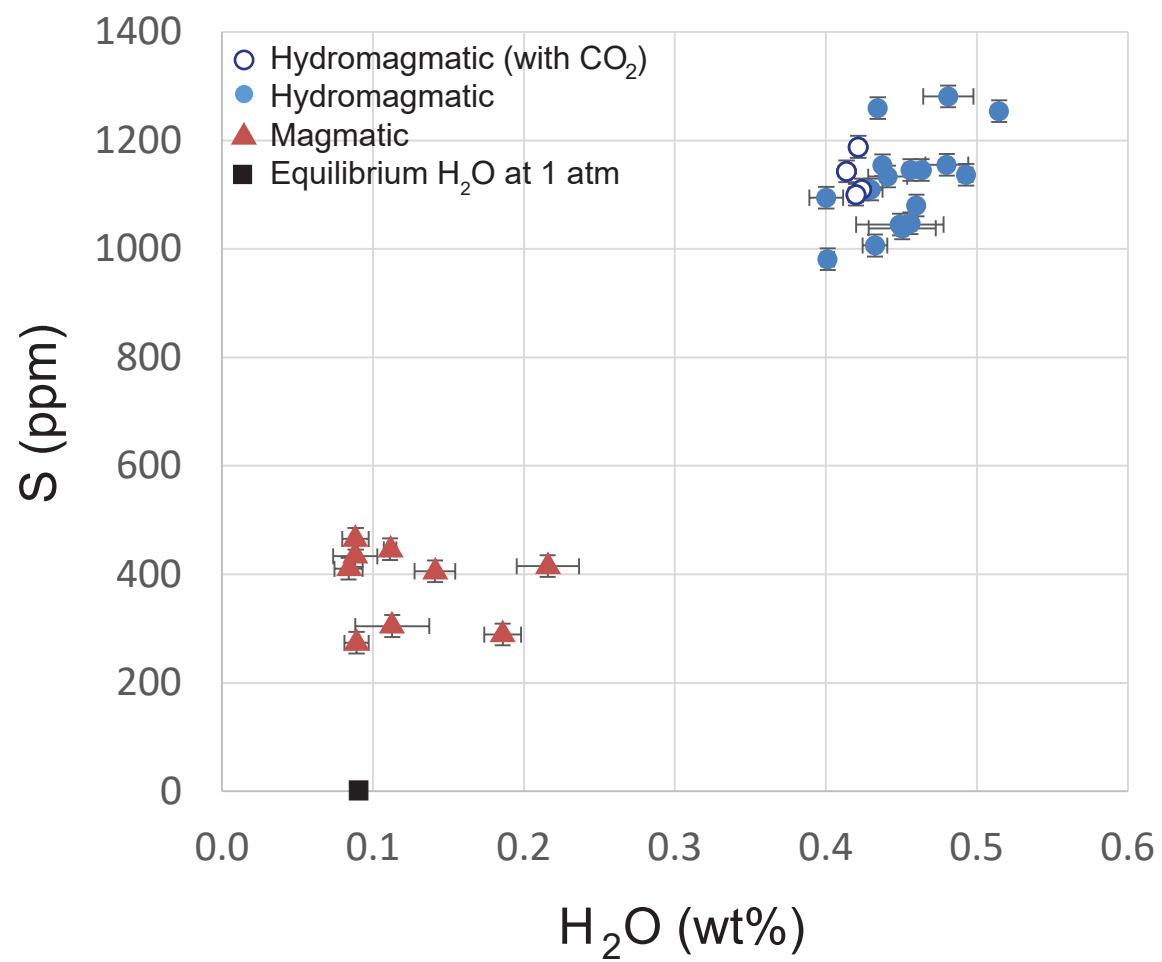


Figure 8

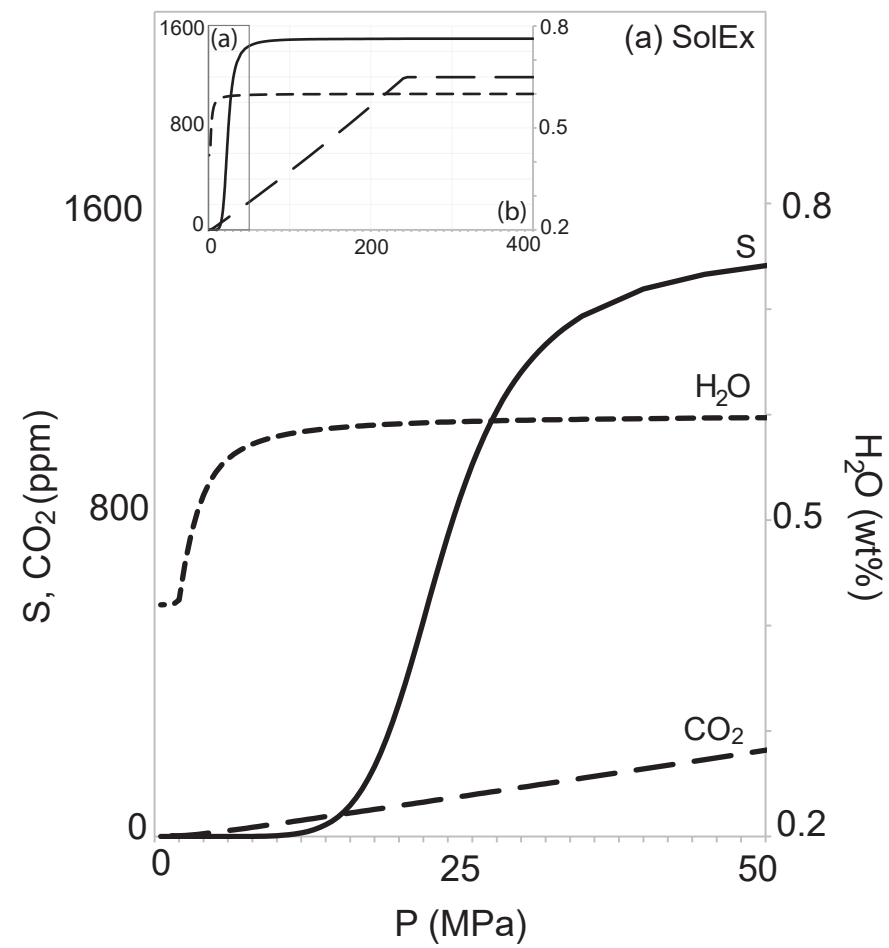


Figure 9

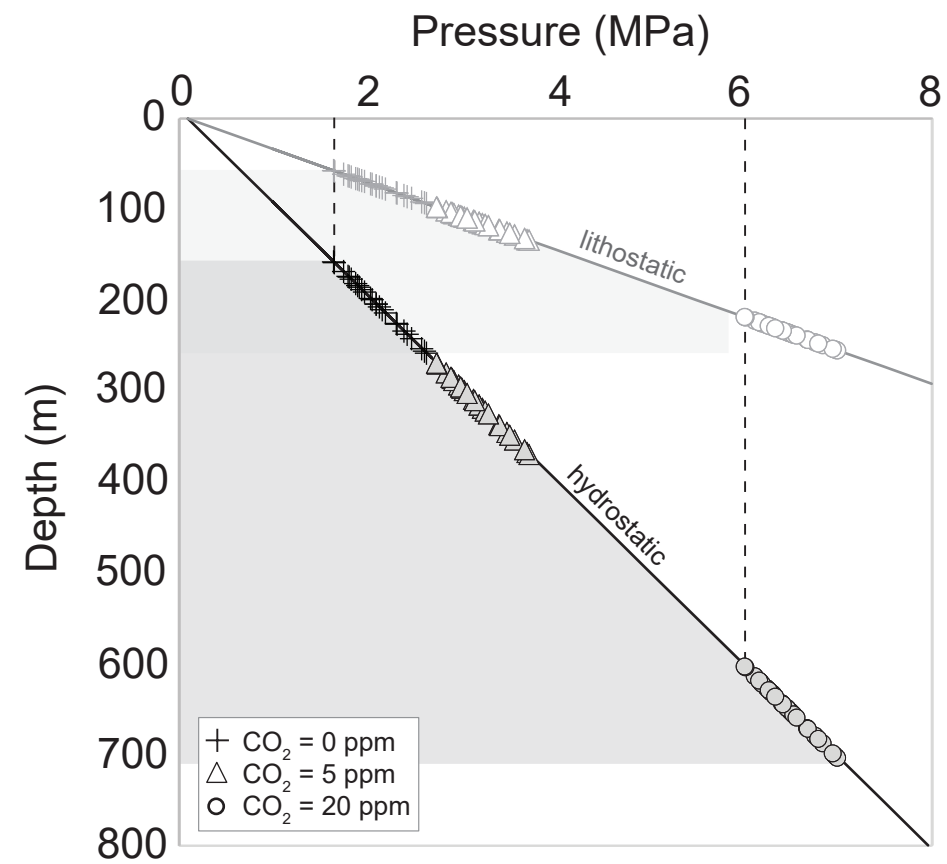


Figure 10

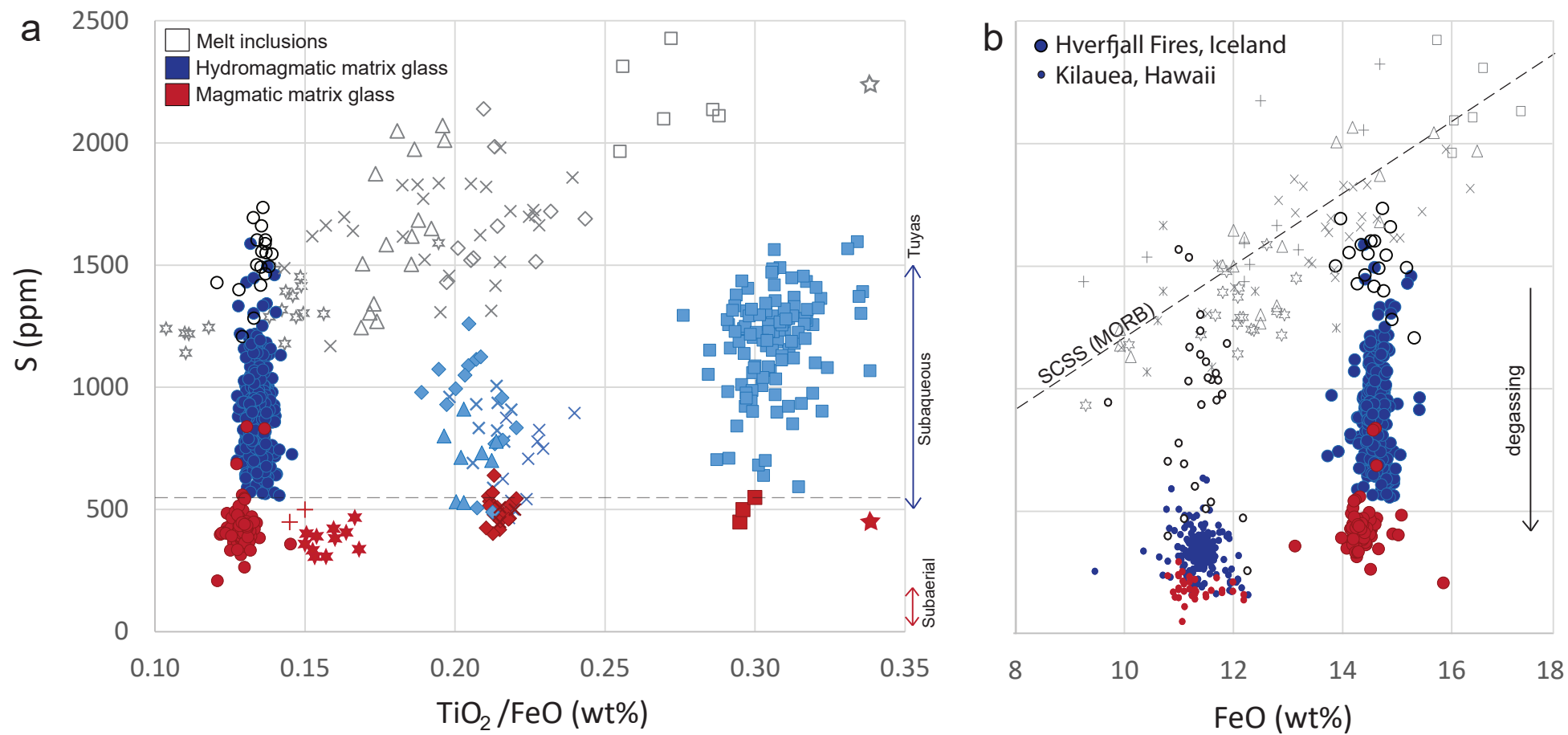
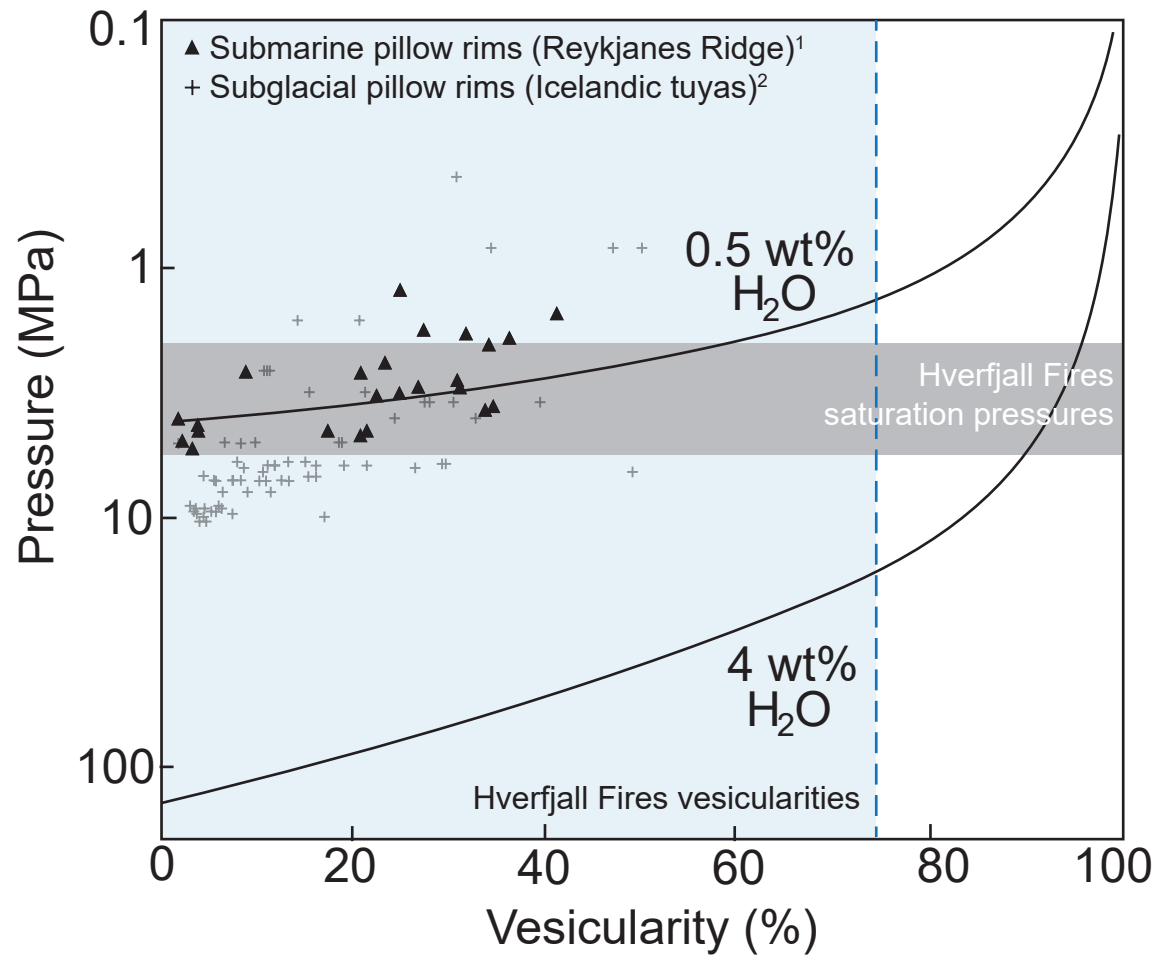


Figure 11



## **Supplementary Information to**

# **“Insights into the dynamics of mafic magmatic-hydromagmatic eruptions from volatile degassing behaviour”**

### **Supplementary Figures**

**Figure S1:** Variation in dissolved water concentration in matrix glass as a function of FTIR wafer thickness. Some, but not all, hydromagmatic glasses thicker than 100  $\mu\text{m}$  contain detectable ( $> 4$  ppm)  $\text{CO}_2$ .

**Figure S2:** Sulfur speciation in hydromagmatic and magmatic matrix glasses, determined by the wavelength shift of the S  $\text{K}\alpha$  peak (Wallace and Carmichael, 1994). The corresponding oxygen fugacities, expressed relative to the fayalite-magnetite-quartz (FMQ) buffer, are calculated according to the calibrations of Jugo et al., (2005; black curve) and Jugo et al., (2010; orange curve); see main text for discussion. Symbols correspond to the dwell times used during data acquisition. The Smithsonian basaltic glass standard VG2 (Juan de Fuca Ridge, NMNH 111240-52) is shown for comparison. Data presented in Table S3, supplementary information.

**Figure S3:** Dissolved sulfur concentration in matrix glasses as a function of particle size.

## Supplementary Tables

**Table S1:** Major element glass compositions expressed as anhydrous oxides, with original totals, for matrix glass and melt inclusions (MI) from hydromagmatic fall, hydromagmatic surge, magmatic fall, and tuff ring crater deposits. All major elements are expressed as weight percent, with the exception of S and Cl, which are shown in ppm. Classification is based on visual observation from backscattered electron SEM images. Ol. = Olivine MI host; Plag. = Plagioclase MI host. Unconsolidated samples are analysed in individual sieved size fractions, whilst the consolidated surge deposits are analysed from thin sections comprising multiple grain sizes. Sample numbers correspond to those given in Table 1.

[see attached text file]

**Table S2:** H<sub>2</sub>O-CO<sub>2</sub> volatile concentrations (from Fourier Transform Infrared Spectroscopy; FTIR) and corresponding major element glass compositions expressed as anhydrous oxides (from electron microprobe) for quenched matrix glasses. All major elements are expressed as weight percent, with the exception of S, Cl and CO<sub>2</sub>, which are shown in ppm. “b.d” indicates below detection (<4 ppm for CO<sub>2</sub>). Full results from FTIR are given in Table S1, supplementary information.

[see attached Excel file]

**Table S3:** Sulfur speciation in matrix glasses and corresponding melt oxygen fugacities ( $fO_2$ ), expressed relative the the FMQ buffer.

[see attached Excel file]

## Appendix A: Sulfur speciation and oxygen fugacity ( $fO_2$ ) in quenched matrix glasses

### A.1 Method

The speciation of sulfur in matrix glasses (samples H<sub>2.3</sub> and M<sub>Q1</sub>; see main text for details) was determined from the wavelength ( $\lambda$ ) of the S  $\alpha$  peak (Carroll and Rutherford, 1988; Wallace and Carmichael, 1994; Jugo et al., 2005; Lesne et al., 2011). Measurements of  $\lambda$ (S  $\alpha$ ) were made using the FEG-EPMA operating under the same conditions as for major element analyses (20 kV, 40 nA), but varying the beam diameter from 10  $\mu$ m (1 s dwell time) to 15  $\mu$ m (100 ms dwell time). For comparison, wavescans were acquired by two methods: (a) 16 static wavescans at 100 ms dwell time for each step; (b) 6 moving wavescans at 1 s dwell time for each step, migrating the beam position by 10  $\mu$ m every 20 s to minimise changes in S speciation due to electron beam exposure (Wallace and Carmichael, 1994; Metrich and Clocchiatti, 1996; Wilke et al., 2008; Metrich et al., 2009).

Wavescan spectra from each method were stacked, and the S  $\alpha$  peak position determined by fitting a Gaussian function to the stacked spectra. The S  $\alpha$  peak positions of FeS<sub>2</sub> (pyrite) and BaSO<sub>4</sub> (barite) standards (representing pure sulfide [S<sup>2-</sup>] and pure sulfate [S<sup>6+</sup>] end-members, respectively) were found to be equivalent for both measurement methods, with an instrumental precision (2 $\sigma$ ; based on 48 spectra per standard) of  $\pm 0.006$  pm (pyrite) or  $\pm 0.015$  pm (barite). The S  $\alpha$  peak position of VG2 basaltic glass standard was also measured.

The oxygen fugacity,  $fO_2$ , of the melt at the point of quenching to glass was calculated from S<sup>6+</sup>/S<sub>total</sub> according to the calibrations of Jugo et al., (2005; from EPMA) and Jugo et al., (2010; from X-ray Absorption Near Edge Structure, [XANES] spectroscopy). The asymptotic relationship between S<sup>6+</sup>/S<sub>total</sub> and  $fO_2$  at low  $fO_2$  imposes a resolution limit of  $\sim$ FMQ +0, below which it is challenging to precisely constrain  $fO_2$  by this technique.



## *A.2 Results*

Sulfur species in matrix glasses from the Hverfjall Fires tephra are sulfide-dominated (Fig. S2; Table S3, supplementary information), with  $S^{6+}/S_{\text{total}}$  ranging from  $<0.11$  (hydromagmatic) and 0.04 to 0.49 (magmatic). The results are independent of the analytical method used (i.e., a moving beam and 1 s dwell time [triangles; Fig. S2] or a static beam and shorter 100 ms dwell time [circles; Fig. S2]). Using the calibration of Jugo et al., (2005), average sulfur speciation values correspond to oxygen fugacities of FMQ  $+0.1 \pm 0.36$  ( $1\sigma$ ; hydromagmatic) and FMQ  $+0.5 \pm 0.72$  ( $1\sigma$ ; magmatic). These  $fO_2$  ranges increase very slightly to FMQ  $+0.4 \pm 0.17$  ( $1\sigma$ ; hydromagmatic) and FMQ  $+0.6 \pm 0.33$  ( $1\sigma$ ; magmatic) if the calibration of Jugo et al., (2010, based on XANES spectra) is used.

## *A.3 References*

- Carroll, M. & Rutherford, M. J. (1988), Sulfur speciation in hydrous experimental glasses of varying oxidation state – results from measured wave- length shifts of sulfur X-rays, *American Mineralogist* 73(7), 845–9.
- Lesne, P., Kohn, S. C., Blundy, J., Witham, F., Botcharnikov, R. E. & Behrens, H. (2011), Experimental simulation of closed-system degassing in the system basalt–H<sub>2</sub>O–CO<sub>2</sub>–S–Cl, *Journal of Petrology* 52 (9), 1737–1762.
- Jugo, P. J., Luth, R. W. & Richards, J. P. (2005), Experimental data on the speciation of sulfur as a function of oxygen fugacity in basaltic melts, *Geochimica et Cosmochimica Acta* 69(2), 497–503.

Jugo, P. J., Wilke, M. & Botcharnikov, R. E. (2010), Sulfur K-edge XANES analysis of natural and synthetic basaltic glasses: Implications for S speciation and S content as function of oxygen fugacity, *Geochimica et Cosmochimica Acta* 74(20), 5926–5938.

Metrich, N. & Clocchiatti, R. (1996), Sulfur abundance and its speciation in oxidized alkaline melts, *Geochimica et Cosmochimica Acta* 60(21), 4151– 4160.

Metrich, N., Berry, A. J., O'Neill, H. S. C. & Susini, J. (2009), The oxidation state of sulfur in synthetic and natural glasses determined by X-ray absorption spectroscopy, *Geochimica et Cosmochimica Acta* 73(8), 2382– 2399.

Wallace, P. J. & Carmichael, I. S. (1994), S speciation in submarine basaltic glasses as determined by measurements of SK $\alpha$  X-ray wavelength shifts, *American Mineralogist* 79, 161– 167.

Wilke, M., Jugo, P. J., Klimm, K., Susini, J., Botcharnikov, R., Kohn, S. C. & Janousch, M. (2008), The origin of S<sup>4+</sup> detected in silicate glasses by XANES, *American Mineralogist* 93(1), 235–240.

Figure S1

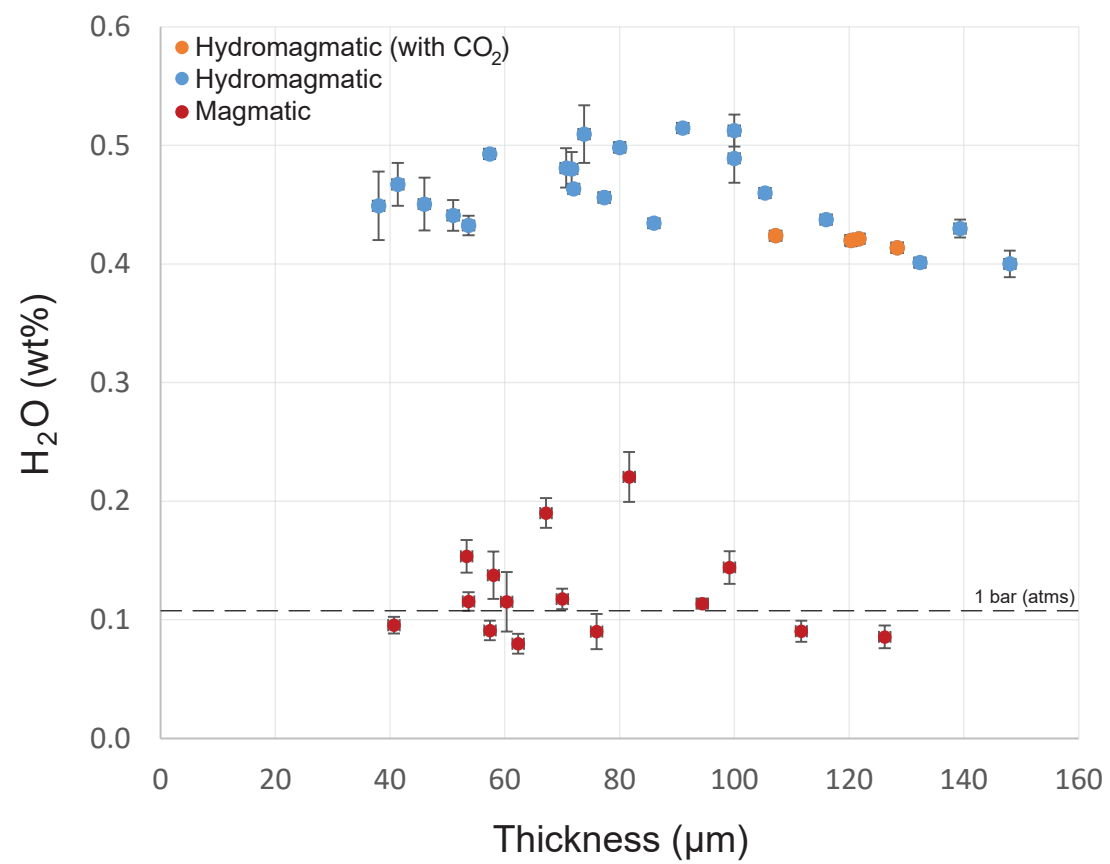


Figure S2

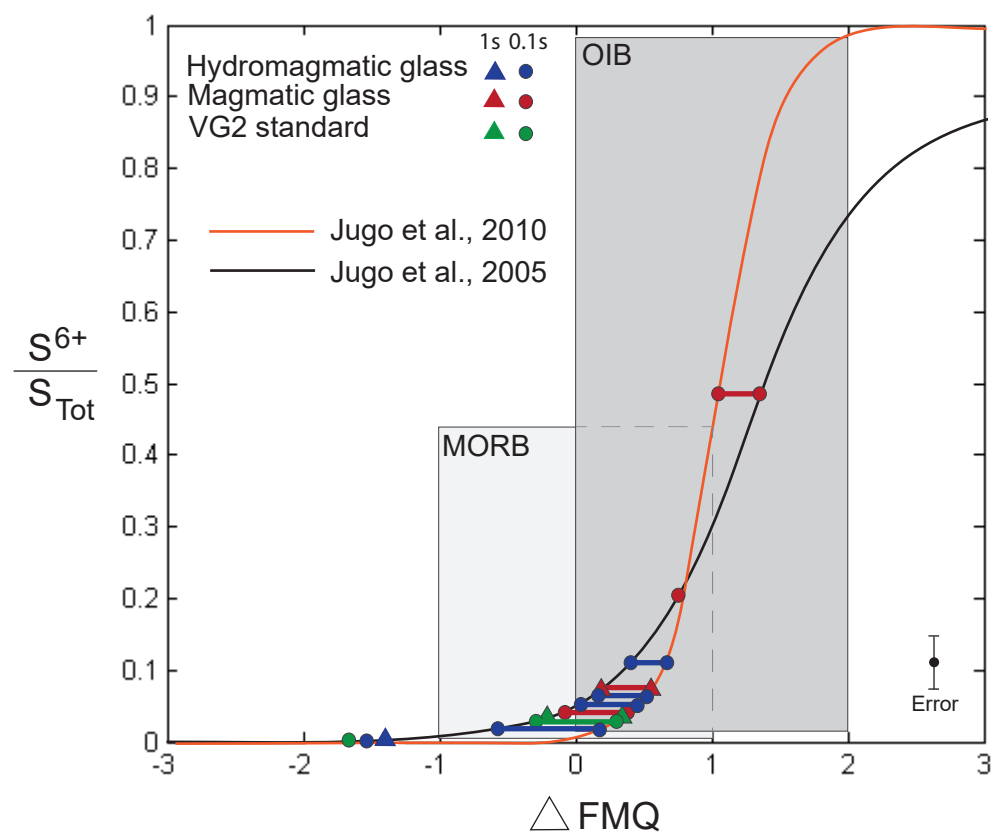


Figure S3

